UNIVERSITY OF CALIFORNIA

Los Angeles

Design-Oriented Modeling and Optimization of On-Chip Inductors

A thesis submitted in partial satisfaction

of the requirements for the degree

Master of Science in Eletrical Engineering

by

Weiyu Leng

2015

ABSTRACT OF THE THESIS

Design-Oriented Modeling and Optimization of On-Chip Inductors

by

Weiyu Leng

Master of Science in Eletrical Engineering

University of California, Los Angeles, 2015

Professor Asad A. Abidi, Chair

The models of CMOS RF inductors are reviewed and improved for design. A compact frequency-independent equivalent circuit is developed for symmetric inductors used in VCOs. The equivalent circuit captures three basic parasitic effects, current crowding, substrate loss, and distributed capacity. All values of LCRM originate from the inductor geometry with a minimum number of fitting parameters.

Simple optimizations are attempted for maximum Q at the operating frequency. Three representative inductors are analyzed using the equivalent circuit. Good agreements have been obtained between the measurement result and the model. The optimization processes prove the optimality of the three sample inductors.

The thesis of Weiyu Leng is approved.

Lieven Vandenberghe

Yuanxun E. Wang

Asad A. Abidi, Committee Chair

University of California, Los Angeles

2015

To my parents

TABLE OF CONTENTS

List of Figures

LIST OF TABLES

ACKNOWLEDGMENTS

I would like to thank my advisor Professor Abidi for guiding me throughout the research. Professor Vandenberghe gave me useful suggestions on the optimization problems related to this work. Thanks to his advice.

Shihan Qin from Professor Wang's group assisted me numerous times on setting up the electromagnetic simulator. I appreciate his help.

Chuan Wang patiently discussed about his understanding of the skin and proximity effects with me. I thank him.

Lastly, My girlfriend Lan Mi supported me mentally throughout the past 12 months. Her encouragement is very important for this research. I am grateful to her.

CHAPTER 1

Introduction

1.1 Background

Although researchers have been searching for inductorless RF solutions recently, on-chip spiral inductors are still widely used in matured RF designs, such as VCOs and LNAs. Aside from the RF domain, more stringent bit-error-rate requirement due to the increasing wireline data rates results in the necessity of using inductors in wireline transceivers. However, compared to other on-chip devices, inductors usually occupy the most area. The high cost of chip area in modern processes urges the optimization of inductors in two aspects. Given a limited area, Can we design an inductor with the highest Q-factor? Alternatively, without sacrificing Q-factor too much, can we minimize the area of an inductor with a fixed inductance. Like all other engineering problems, optimization starts from good models.

1.2 Literature Review

The modeling of on-chip inductors has been studied intensively since 1990s, when Meyer realized the first integrated inductor [4]. There are generally three types of models, distributed models, frequency dependent models, and compact frequency independent models. Distributed models, such as [5], are very accurate but unnecessarily complicated. Frequency dependent models [6, 7, 8, 9, 1] are unphysical and can only be applied at one frequency. Compact frequency independent models [10, 11, 12, 13, 14, 15] combine simplicity and accuracy, which offer the most insight and are thus widely

adopted by designers. The frequency independent model is developed via either parameter fitting based on electromagnetic simulations (EMS) or direct calculation from physical geometries. Although parameter fitting provides better agreement with the inductor which is treated as a black box, the process is very sensitive to small errors. Some fitted values of the circuit elements could depart far from reality merely to minimize the mean-square error. The lack of linkage between the fitted equivalent circuit and actual physics turns this modeling method useless for designers. On the other hand, the latter method calculates each circuit element based on physics of the inductor, turning the circuit model useful for design. In this work, we hence focus on physics-based frequency independent model.

The optimization of inductors was first studied in [16] using geometric programming. Later works used other optimization algorithms, such as discrete variable search [17] and sequential quadratic programming [18]. There were two common problems in these works. Firstly, most attention was put onto the optimization algorithms, which could not explain why an inductor was optimal. In reality, the optimization problem related to inductors only has $3 \sim 4$ variables if defined properly, so complicated searching algorithms may not be needed. Secondly, the equivalent circuits used in those works were either complicated or inaccurate. This work will apply the idea of optimization using the improved physical frequency independent equivalent circuit.

1.3 Structure of This Work

Ch. 2 lists all the relevant equations for inductances and magnetics. Ch. 3 introduces the construction of the physics-based equivalent circuit, in terms of the series loss, the substrate parasitics, and the inter-winding capacitance. Ch. 4 clarifies and compares the definitions of the Q factor. Three example inductors are studied using the model in Ch. 5.

CHAPTER 2

Formulas for Inductances and Magnetics

2.1 Inductances of Filaments

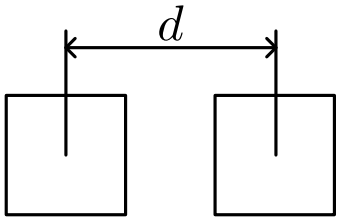

Figure 2.1: Two Coupled Straight Conductors

The mutual inductance of two straight conductors of length l ($\frac{l}{d} \gg 1$) with square cross section can be calculated according to the definition of the geometric distance [19] and the formula in [20] (Fig. 2.1).

$$M \approx \frac{\mu_0}{2\pi} l \left[ln\frac{2l}{d} - 1 \right] \approx \frac{\mu_0}{2\pi} l \cdot ln\frac{2l}{d}. \tag{2.1}$$

The self-inductance of a single straight rectangular conductor of width a and thickness b can be calculated by

$$L = \frac{\mu_0}{2\pi} l \left[ln\frac{2l}{0.2235(a+b)} - 1 + \frac{0.2235(a+b)}{l} \right] \approx \frac{\mu_0}{2\pi} l \cdot ln\frac{2l}{0.2235(a+b)}. \tag{2.2}$$

(2.1) and (2.2) will be useful for the modeling of distributed effects such as the skin effect and the proximity effect.

2.2 Mechanism of the Spiral inductor

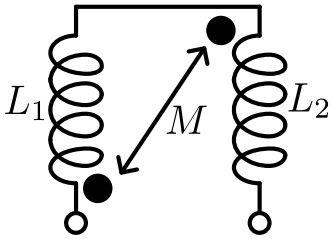

Figure 2.2: Conceptual Equivalent Circuit of a Two-turn Spiral

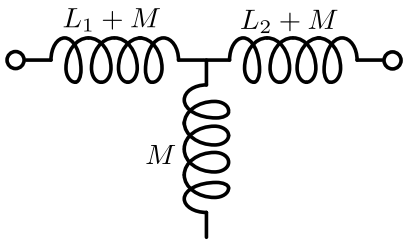

Figure 2.3: T-π Transformed Equivalent Circuit of Fig. 2.2

A multi-turn inductor takes advantage of the positive mutual coupling between turns. Fig. 2.2 illustrate the principle of positive mutual coupling. For a two turn inductor, the first turn and the second turn are modeled by L_1 and L_2 respectively, and the mutual inductance between them can be modeled by M. Since the L_1 and L_2 are in series, the equivalent circuit can be transformed into a T-network shown in Fig. 2.3. As a result, an extra inductance of $2M$ is added onto $L_1 + L_2$, which means that a shorter length of metal is necessary for a given total inductance. If the mutual coupling coefficient between any pair of turns in a multi-turn inductor were 1, the inductance could be theoretically proportional to N^2. However, the finite width and spacing of an inductor limit the coupling coefficient between adjacent turns to some value under 0.75. The coupling coefficients between non-adjacent turns are even smaller. Thus, the inductance increase sub-quadratically as a function of N.

2.3 The formula for DC inductance

The most accurate way to calculate the inductance is the Greenhouse's Method[21], which essentially uses the idea summarized in Ch. 2.2. However, Greenhouse's Method is tedious and cannot be programed into the optimization algorithm easily. Numerous works have presented compact formulas of the DC inductance with measurable vari-

ables such as diameter(d_{in}, d_{out}), trace width w, number of turns N, and spacing s. In this work, the formulas from [22] are used:

$$L = \frac{\mu_0 N^2 d_{avg}}{2}\left(ln\frac{2.46}{\rho} + 0.2\rho^2\right), \tag{2.3}$$

where

$$d_{avg} = \left\langle d_{in}, d_{out} \right\rangle \tag{2.4}$$

$$\rho = \frac{d_{out} - d_{in}}{d_{out} + d_{in}}. \tag{2.5}$$

Note that (2.3) uses the fill ratio ρ as a discrepancy factor to capture the sub-quadratic dependence of the inductance on N.

2.4 Off-axis Fields Arising from a Loop of Current

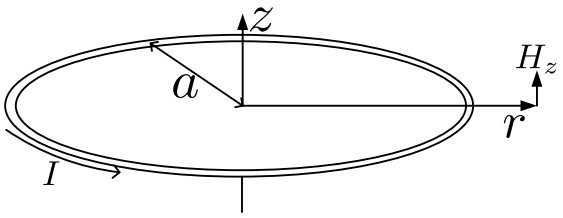

Figure 2.4: A Loop of Current

The general expression of the vertical **H** fields on the plane where a loop of current lays can be written in the following way, whose the variables are shown in Fig. 2.4 [23]:

$$H_z = \frac{2I}{\sqrt{Q}}\left[F(k) + \frac{a^2 - r^2}{Q}\frac{E(k)}{1-k^2}\right], \tag{2.6}$$

where

$$Q = a^2 + r^2, \tag{2.7}$$

$$k = \sqrt{\frac{4ar}{(a+r)^2}}. \tag{2.8}$$

F and E are elliptic integral of the first and the second kind, respectively. These equations will be useful in modeling the proximity effect.

CHAPTER 3

Construction of the Equivalent Circuit

3.1 Revisiting Skin and Proximity Effects

At high frequency, the current in a conductor does not distribute evenly. This current crowding effect is a well-known distributed effect that cannot be modeled fully with finite number of frequency-independent circuit elements. The mechanism of current crowding is the same as that of the current division in a parallel RC network. If a sinusoidal-steady-state current stimulus is forced to an impedance, the current is going to divide between R and C such that the driving point impedance $|(R||\frac{1}{j\omega C})|$ is minimized.

Consider a loop of conductor excited by a sinusoidal-steady-state current source (Fig. 3.1). The current can flow through any part of the conductor. According to Ampere-Faraday's Law, the back emf created by the changing magnetic flux encircled by the conductor can be modeled as an inductor L. The finite resistivity of the conductor can be modeled as a series resistor R. At low frequency, R dominates, and the current will flow uniformly such that $R \approx |Z_{in}|$ is minimized. When the frequency increases, ωL starts to dominate R, so the current will tend to flow around the inner loop to minimize the enclosed flux and thus ωL. This comes at a price of increasing R, because the current flows through less cross-section area than it does at low frequency. However, the increase in R is still desensitized by ωL, even if L is decreased (Fig. 3.2). Hence, the overall impedance $|R + j\omega L|$ is minimized.

There are two kinds of current crowding effects, the skin effect and the proximity

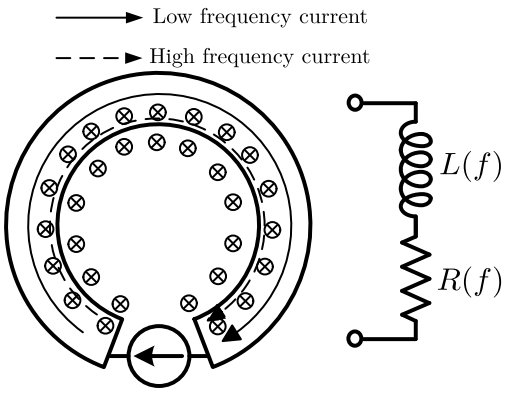

Figure 3.1: Loop Conductor and Equivalent Circuit

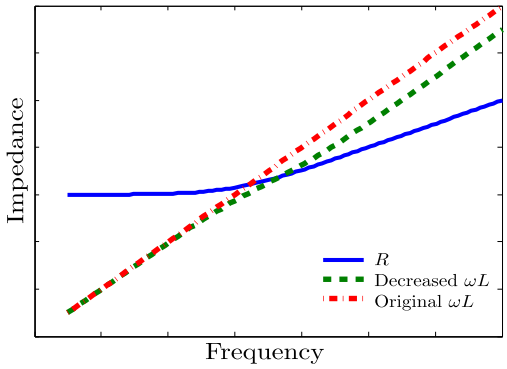

Figure 3.2: Illustration of the Impedance

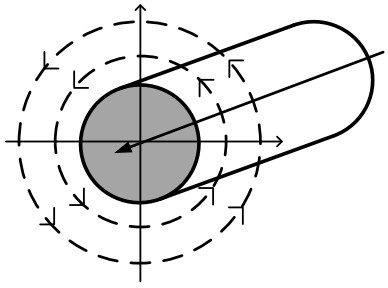

Figure 3.3: A Single Conductor

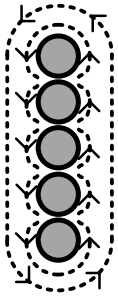

Figure 3.4: Bundled Conductors

effect. The following definitions for these two effects are summarized and generalized based on the definition given in [24].

The skin effect is the redistribution of currents in a straight single conductor or a group of bundled conductors. The magnetic field distribution, before or after the onset of skin effect, is always spatially odd. The distribution of currents is always spatially even. The return path of the straight conductors is the whole space at infinity. Fig. 3.3 shows a simple example of a straight circular conductor with its odd magnetic fields. Fig. 3.4 presents an extended example of straight conductors.

The proximity effect is the emergence of eddy currents in a non-current-carrying straight conductor or a group of bundled conductors due to an externally applied field.

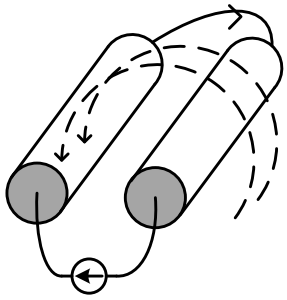

Figure 3.5: External Magnetic Field Caused by Winding

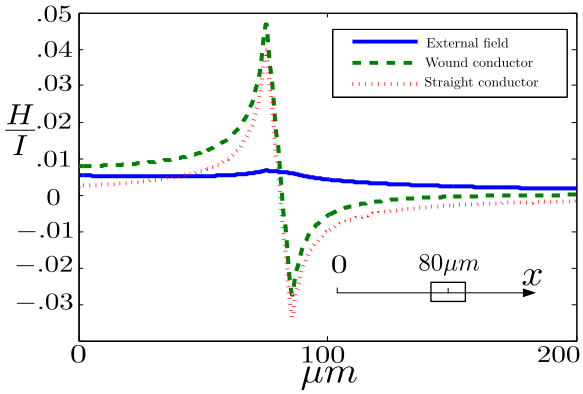

Figure 3.6: A Numerical Example of Fig. 3.5

The externally applied field is an imaginary term for the ease of modeling. In reality, the external field is effectively caused by winding up a straight conductor (Fig. 3.5). In general, the external field due to winding is not uniform. Fig. 3.6 shows the vertical **H** fields normalized to I of a $10\mu m$ wide conductor when left straight or wound up to a loop of radius $80\mu m$. The difference between the **H** fields under these two conditions is the external field due to winding.

The concept of the AC resistance R_{ac} is essential in understanding the current crowding effect. Consider a rectangular conductor carrying a non-uniform sinusoidal-steady-state current. The distribution of the current can be described by current density $J = J_0 e^{j\omega t}$ as a function of position. The total average power per unit length can be expressed as

$$P_{av} = \left\langle \int_A Re(J_0 e^{j\omega t}) \cdot Re(J_0 e^{j\omega t}) \cdot \rho \; dA \right\rangle = \frac{\rho}{2} \int_A \cdot J_0 \cdot \overline{J_0} \; dA = \frac{1}{2} |I|^2 \cdot R_{ac}, \qquad (3.1)$$

where

$$I = \int_A J_0 \; dA. \qquad (3.2)$$

Hence, R_{ac} is defined as an effective resistance which carries the same total current as the original conductor does and consumes the same amount of power. In light of this definition, the overall current distribution can be classified into a spatially odd part and

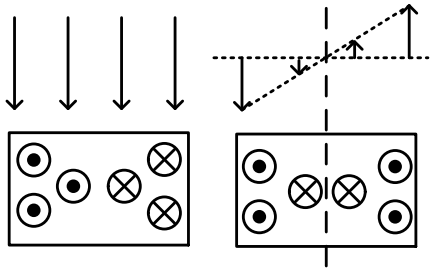

Figure 3.7: Even Mode Proximity Effect (left) and Odd Mode Proximity Effect (right)

a spatially even part [25]:

$$P_{av} = \frac{\rho}{2}\int_A (J_{even}+J_{odd})(\overline{J_{even}}+\overline{J_{odd}})\,dA = \frac{\rho}{2}\int_A |J_{even}|^2\,dA + \frac{\rho}{2}\int_A |J_{odd}|^2\,dA \quad (3.3)$$

$$\int_A J_{odd}\cdot\overline{J_{even}}\,dA = 0, \quad (3.4)$$

because $J_{odd}\cdot\overline{J_{even}}$ is an odd function across the area of integration.

As discussed previously, the skin effect only causes even mode loss, since the current distribution is always even, but the proximity effect is somewhat complicated. Fig. 3.7 illustrates the difference between an even mode proximity effect and an odd mode proximity effect. The odd proximity effect induces an even mode loss in the conductor, which is no longer orthogonal to the even skin effect loss. If the externally applied field is vertical to the conductor, there is a Taylor expansion of the magnitude of the field as a function of the horizontal position. The even terms will cause odd mode loss, while the odd terms will cause even mode loss. If the higher order terms in that Taylor series can be neglected, and only zeroth-order term remains, the proximity effect loss is orthogonal to the skin effect loss and can be modeled separately. In typical on-chip inductor windings with multiple turns, it is good enough to assume that the there is a uniform magnetic field applied vertically to each turn, which is caused by the winding. The magnitude of that uniform field is the average value of the total magnetic field across the width of each turn. Note that if a single conductor is straight and isolated, the average of the vertical magnetic field will be zero, which goes back to

the pure skin effect case. Numerous publications have separated the skin effect and the proximity effect, but the explanation and justification of their approximations are given here.

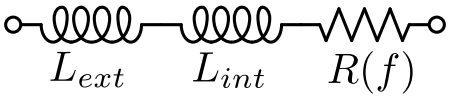

Figure 3.8: Conceptual Equivalent Circuit for a Conductor

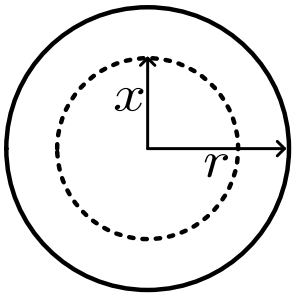

Figure 3.9: Nomenclatures for Calculation

Besides the change in the real part of the impedance at high frequency, conductors also have slightly lower effective inductance at high frequency. This effect will directly guide the construction of the equivalent circuit for the skin effect and the proximity effect. To begin with, the distinction between the internal inductance and the external inductance should be clarified. The internal inductance L_{int} models the magnetic energy stored by the magnetic field within the conductor. The external inductance L_{ext} simply captures all the magnetic energy stored outside of the conductor, as if all the currents are flowing on the surface of the conductor. (Fig. 3.8)

Fig. 3.9 shows a long circular straight wire carrying a uniformly distributed current. The H field in the conductor can be found by Ampere's Law to be

$$H(x) = \frac{1}{2\pi} \cdot \frac{x}{r^2} I. \tag{3.5}$$

The total magnetic energy in the conductor per unit length is then

$$E_m = \frac{1}{2}\mu_0 \int_0^{2\pi} \int_0^r \left(\frac{1}{2\pi} \cdot \frac{x}{r^2} I\right)^2 dx d\theta \tag{3.6}$$

$$= \frac{1}{2}\frac{\mu_0}{8\pi} \times I^2 \tag{3.7}$$

$$= \frac{1}{2} L_{int} I^2 \tag{3.8}$$

Then, $L_{int} = 50nH/m$ at DC.

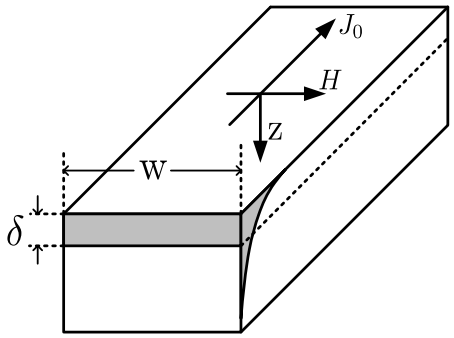

Figure 3.10: A Semi-infinite Slab

Consider the same long straight wire under full skin effect. Since all currents flow on the surface of the wire, the wire can be seen as a semi-infinite slab with all the currents clinging on the top (Fig. 3.10). Solving EM equations with proper boundary conditions reveals the current distribution:

$$J(z) = J_0 e^{(-(1+j)\frac{z}{\delta})}, \tag{3.9}$$

where δ is the skin depth of the material. The total current can be integrated as

$$I = w\int_0^\infty J\,dz = \frac{J_0 w\delta}{1+j} \tag{3.10}$$

R_{ac} can be calculated by (3.1) as $\frac{\rho}{w\delta}$. The H field within the slab will be

$$H(z) = \int_z^\infty J_0 e^{(-(1+j\frac{z'}{\delta}))}\,dz' \tag{3.11}$$

$$= J_0 \cdot \frac{\delta}{1+j} \cdot e^{(-(1+j)\frac{z}{\delta})}. \tag{3.12}$$

The total stored magnetic energy per unit length can then be calculated:

$$\mu_0 \int_A |H|^2\,dA = \mu_0 w \int_0^\infty J_0^2 \frac{\delta^2}{2} e^{-\frac{2z}{\delta}}\,dz \tag{3.13}$$

$$= \mu_0 w J_0^2 \cdot \frac{\delta^2}{2} \cdot \frac{\delta}{2} \tag{3.14}$$

$$= L_{int} \cdot \frac{J_0^2 w^2 \delta^2}{2} \tag{3.15}$$

Then,

$$L_{int} = \frac{\mu_0}{w}\frac{\delta}{2} = \frac{R_{ac}}{\omega} \tag{3.16}$$

$$\omega L_{int} = R_{ac}. \tag{3.17}$$

Hence, when the skin effect is felt fully in a circular wire, the internal impedance $Z_{int} = R_{ac} + j\omega L_{int}$ has a phase of 45° and a magnitude proportional to $\sqrt{f}$. In [26], Wheeler reached the same conclusion using the Transmission Line Theory and generalized this result for any conductor with a smooth surface. Nevertheless, when the shape of the conductor is rectangular, no simple method can be applied to find the DC internal inductance or the relationship between R_{ac} and ωL_{int} at high frequency. [27] used numerical methods based on the magnetic Green's Function to find the total magnetic energy within the rectangular conductor and thus the DC internal inductance per unit length as a function of the aspect ratio $\frac{t_m}{w}$ (Fig. 3.11). (3.18) provides a fitted polynomial to the curve.

$$\frac{L_{int}}{l} = 0.045 + 200\frac{t_m}{w} - 443\frac{t_m}{w}^2 + 724\frac{t_m}{w}^3 - 824\frac{t_m}{w}^4 + 537\frac{t_m}{w}^5 - 147\frac{t_m}{w}^6 \quad \left(\frac{nH}{m}\right) \tag{3.18}$$

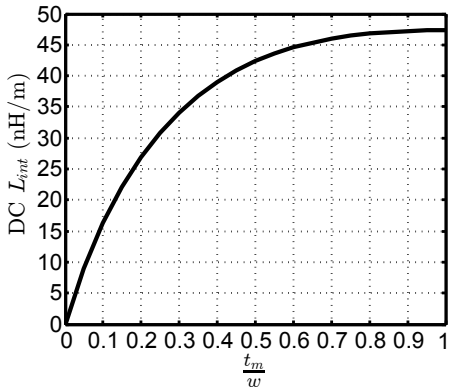

Figure 3.11: L_{int} of Rectangular Conductors at DC

[28] used similar numerical methods to find the relationship between R_{ac} and ωL_{int} at high frequency. The results show that the phase angle is always beteen 30° and 45° for all aspect ratios, and $|Z_{int}|$ at high frequency is still proportional to $\sqrt{f}$.

Although [28] did not give a closed-form solution of the phase of Z_{int} at high frequency, it is actually unnecessary to do so. Fig. 3.11 shows that the DC L_{int} of a rectangular conductor never exceeds $50nH/m$, which is much smaller the total DC inductance ($L_{ext} + L_{int}$) of almost any conductor. This indicates that $L_{ac} \approx L_{ext}$ even at infinite frequency, when L_{int} is lost completely due to the skin effect. Hence, it is only necessary to model R_{ac} accurately in the subcircuit for the skin effect. The phase of the impedance of the subcircuit can be chosen to be anywhere between 30° and 45°.

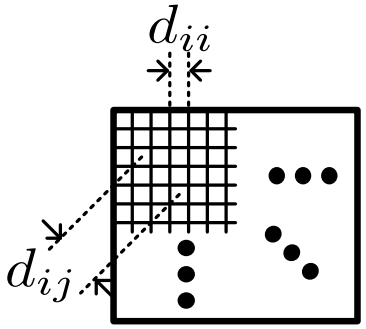

Figure 3.12: Filaments of A conductor

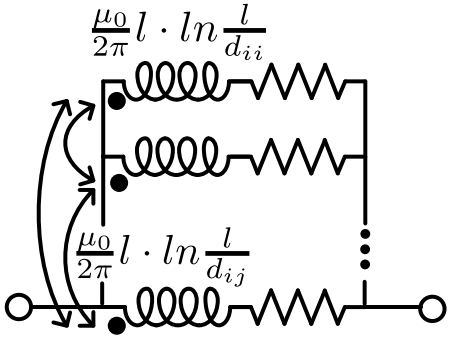

Figure 3.13: Modal Network

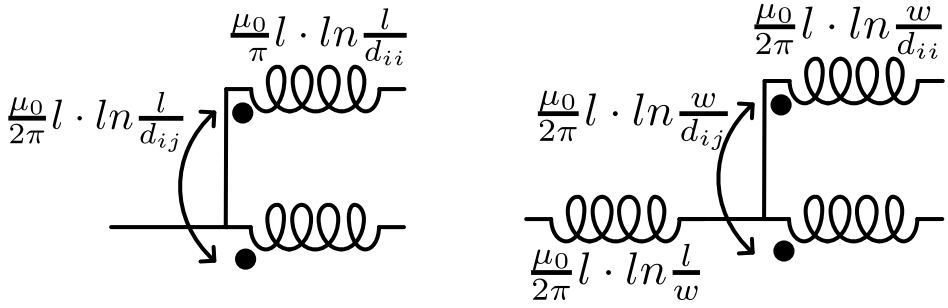

Figure 3.14: Transformation of the Modal Network so that All Elements ∝ Length

Since R_{ac} is more important than L_{int} in describing the skin effect, an accurate way of estimating the resistance ratio $\frac{R_{ac}}{R_{dc}}$ is needed for the development of the subcircuit. In [29], Silvester proposed the Modal Network Theory to calculate R_{ac} for rectangular conductors. Briefly, a long conductor is divided into small parallel filaments in which the currents are uniform (Fig. 3.12). The self and mutual inductances of those filaments

can be calculated using (2.2) and (2.1), and the modal network is shown in Fig. 3.13. Since a common inductance of any value can be subtracted from all the $L's$ and $M's$ in the parallel network and added in series, all $L's$, $M's$ and $R's$ in the new parallel network are proportional to length l (Fig. 3.14). The common inductance in series can be discarded, because only the parallel branches with resistors can contribute to the real part of the total impedance. R_{ac} per unit length can then be found by solving the network matrix. The Modal Network Theory is completely general for any aspect ratios of the rectangular conductors. However, it is computationally too expensive to divide the rectangular conductors into filaments every time and solve large matrices. In dealing with skin-effect problems, it is often convenient to make use of the principle of similitude [30]. The principle states that $\frac{R_{ac}}{R_{dc}}$ is only a function of a normalized variable $\frac{\sqrt{A}}{\delta}$. In this work, a scaling factor $\sqrt{\frac{2}{\pi}}$ is added to match the results presented in [30]. Then, the universal curves can be plotted as a function of the normalized variable $x = \sqrt{\frac{2}{\pi}} \times \frac{\sqrt{A}}{\delta}$ for different aspect ratios $\frac{w}{t_m}$.

Since the dimensions of on-chip interconnects are on the order of μm, it is customary to pick the filament dimension to be $0.1\mu m \times 0.1\mu m$. To apply the Model Network Theory, the skin depth should be greater than $0.2\mu m$, such that the current within the filament is roughly uniform. The upper limit of x for on-chip inductors is picked according to the worst case geometry. The thickness of top metal in modern RF CMOS processes are smaller than $4\mu m$, and the width of inductor traces rarely exceeds $40\mu m$. The skin depth at $10GHz$ for copper is $0.662\mu m$. Then,

$$x_{max} = \sqrt{\frac{2}{\pi}} \times \frac{\sqrt{40 \times 4}}{0.662} \approx 15 \tag{3.19}$$

Back to the filament model,

$$\sqrt{\frac{2}{\pi}} \times \frac{\sqrt{w \times t_m}}{0.2} \geq 15 \tag{3.20}$$

$$\sqrt{w \times t_m} \geq 4\mu m \tag{3.21}$$

A MATLAB program is written to calculate $\frac{R_{ac}}{R_{dc}}$ for all the cases listed in Table 3.1. The results are plotted in Fig. 3.15. Note that at very high frequency, the currents in

a rectangular conductor will concentrate more on the edges, so R_{ac} will be larger than $\frac{\rho}{2\cdot\delta(w+t_m)}$, which is captured by a scaling factor k on the order of $1.3 \sim 1.8$ [30].

Table 3.1: Test Cases for the Universal Curves of Skin Effect

$\frac{w}{t_m}$	w	t_m	k	Asymptote at Very High Frequency
1	5	5	1.32	$0.414x$
2	7	3.5	1.3	$0.384x$
4	10	2.5	1.35	$0.338x$
8	16	2	1.5	$0.295x$
16	24	1.5	1.7	$0.243x$
25	25	1	1.75	$0.211x$

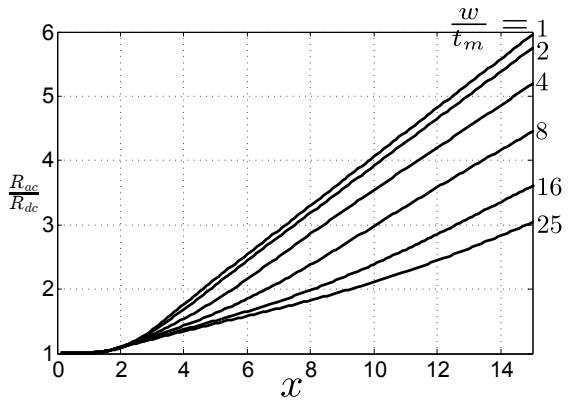

Figure 3.15: Universal Curves of $\frac{R_{ac}}{R_{dc}}$ for Different Aspect Ratios

The universal curves in Fig. 3.15 guide the design of the equivalent subcircuit for the skin effect. $Z_{int} \propto \sqrt{f}$ after the onset of skin effect, but no circuit element can give an impedance with a $\sqrt{f}$ dependency.

In [31], a RC ladder circuit was synthesized to expand the tuning range of a relaxation oscillator (Fig. 3.16). The input impedance Z of the RC ladder has alternating poles and zeros, so the asymptote of $|Z|$ is a segmented line whose slope is alternating between 0 and -1 (Fig. 3.17). Specifically, If the horizontal segments extent half of the

range as that of the tilted segments, the net curve will have a slope of $-2/3$ approximately [31]. At very high frequency, the resistors at all ladders are in parallel, and $|Z|$ converges to $R_0||R_1||R_2||R_3$. The phase of Z is 0^o at DC or very high frequency. At intermediate frequencies, the phase angle stays at a constant value depending on the relative spacings of poles and zeros.

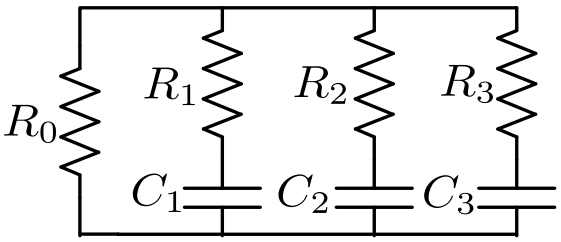

Figure 3.16: RC Ladder

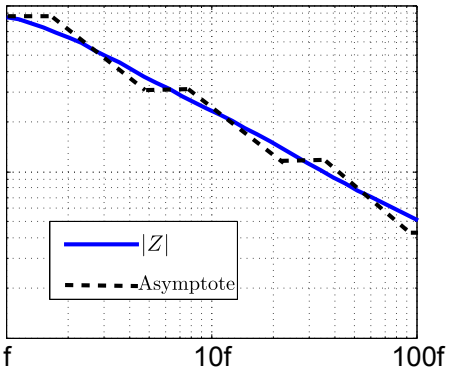

Figure 3.17: Impedance of RC Ladder

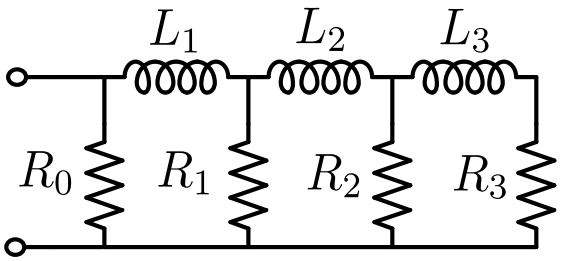

Figure 3.18: Cauer Type LR Ladder

As discussed previously, the internal impedance of a conductor Z_{int} has a magnitude proportional to $\sqrt{f}$ and a constant phase angle $< 45^o$. The concept of synthesizing a ladder network to give a non-integer-frequency-dependent impedance can be used to model Z_{int} of a conductor. Fig. 3.18 shows the counterpart of the RC ladder network in, an LR ladder [32]. Once the positions of the three poles and three zeros of the input admittance are known, all $L's$ and $R's$ in the ladder can be calculated by the Cauer Type Synthesis method. Previous calculations show that $Im(Z_{int})$ is less important than

$Re(Z_{int})$. As long as the phase of Z_{int} is less than 45^o, $Im(Z_{int})$ is always dominated by ωL_{ext}. Hence, only $Re(Z_{RL})$ needs to be fitted to R_{ac}. Curve fitting tools shall be used to calculate the most suitable positions of poles and zeros. Nevertheless, in this work, example positions of poles and zeros as a function of conductor's geometry are empirically proposed to fit the universal curves in Fig. 3.15. (3.22) - (3.25) lists all the related estimation of poles and zeros for different aspect ratios. Future work might be necessary to give a more accurate prediction of the positions of poles and zeros as a function of the conductor's geometry, but this work still demonstrates a theoretically correct approach to model the skin effect.

$$\omega_{z1} = 2\pi\sqrt{\frac{w}{t_m}} \cdot \frac{2^2\rho}{2wt_m \cdot \mu}, \tag{3.22}$$

$$\omega_{p3} = 2\pi\frac{15^2\rho}{2wt_m \cdot \mu}, \tag{3.23}$$

$$\chi = \left(\frac{\omega_{p3}}{\omega_{z1}}\right)^{\frac{1}{5}}, \tag{3.24}$$

$$\omega_{p1} = \chi\omega_{z1},\ \omega_{z2} = \chi^2\omega_{z1},\ \omega_{p2} = \chi^3\omega_{z1},\ \omega_{z3} = \chi^4\omega_{z1}, \tag{3.25}$$

$$Z_{int} \approx Z_{LR} = R_{dc}\frac{(1+\frac{s}{\omega_{z1}})(1+\frac{s}{\omega_{z2}})(1+\frac{s}{\omega_{z3}})}{(1+\frac{s}{\omega_{p1}})(1+\frac{s}{\omega_{p2}})(1+\frac{s}{\omega_{p3}})}. \tag{3.26}$$

L_{ext} can then be added in series with the LR ladder to model the conductor completely.

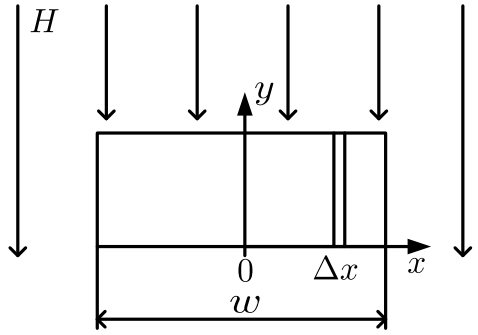

Figure 3.19: Setup for Proximity Effect Calculations

The proximity effect can also be modeled by the equivalent circuit. Since the magnetic field applied on each turn of the inductor can be model as uniform, the dependence of the odd mode loss on frequency can be determined, and the corresponding equiva-

lent circuit can be constructed. Based on Dowell's Method [33], consider a rectangular conductor subject to a vertical uniform **H** field, as shown in Fig. 3.19. Although the induced odd mode eddy current density is not necessarily only a function of the horizontal position x, neglecting its dependency on y significantly reduces the complexity of calculation and reveals important insights. Due to geometric symmetry, only the current distribution within half of the conductor needs to be modeled. The current distribution in the other half will simply be the anti-symmetric version. At x, the total flux to the left of x due to the current to the right of x is defined as $\phi(x)$. At $x+\Delta x$, the flux will increase by an incremental amount

$$\Delta\phi = -\mu_0 \cdot H \cdot \Delta x \cdot l_{tt}, \tag{3.27}$$

where l_t is the total length of the conductor. The voltage across every incremental layer in Fig. 3.19 is

$$V = J\rho l_{tt} + j\omega\phi(x). \tag{3.28}$$

Since all the incremental layers are in parallel, (3.28) should not depend on x, so

$$\frac{dV}{dx} = 0 = \rho l_{tt}\frac{dJ}{dx} + j\omega\frac{d\phi}{dx}. \tag{3.29}$$

The **H** field at x can be calculated by

$$H = \int_0^x J(x')dx' = -\frac{\Delta\phi}{\Delta x}\cdot\frac{1}{\mu_0 l_{tt}}. \tag{3.30}$$

(3.30) and (3.29) implies that

$$\frac{d^2J}{dx^2} = \Big(\frac{j\omega\mu_0}{\rho}\Big)J \tag{3.31}$$

(3.31) is the classic 1-D Helmholt Equation. [33] and [34] contain the detailed process of solving this equation using proper boundary conditions and general solutions. [35] conclude the results by introducing a proximity loss factor such that

$$P_{prox} = G|H|^2\rho \tag{3.32}$$

where P_{prox} is the power loss due to proximity effect per unit length. The externally

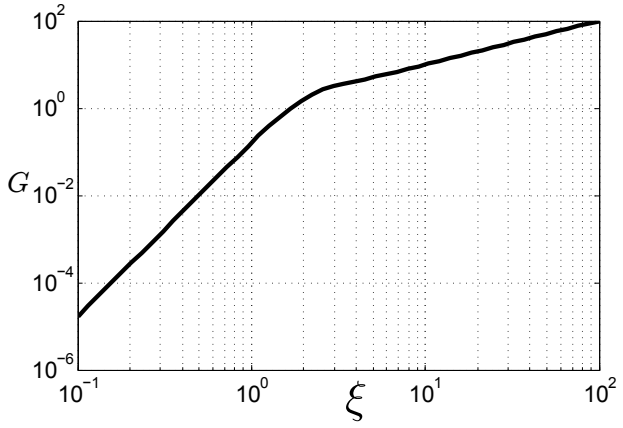

Figure 3.20: Proximity Factor

applied field **H** and ρ are both constant, and G is a function of another similitude variable $\xi = \sqrt{\frac{\pi}{4}} \cdot \frac{w}{\delta}$ (Fig. 3.20). Note that the slope of G is 4 when $\xi \ll 2$ and is 1 when $\xi \gg 2$. Since $\xi \propto \sqrt{f}$, it can be concluded that the proximity effect loss is proportional to f^2 when the $\delta \gg w$ and is proportional to $\sqrt{f}$ when $\delta \ll w$. In [34], plots of current density as a function of x show that the eddy current due to proximity effect tends to cling to the two sides of the conductor. At low frequency, the eddy current density decreases linearly from the sides to the center. At high frequency, the eddy current density decays exponentially from the sides to the center and can be approximated as a uniform current of thickness δ. [36] also reached this result using basic electromagnetic equations.

In [13], a coupled LR circuit was introduced to model the frequency dependence of proximity effect loss (Fig. 3.21). The mutual inductance M_{eddy} captures the magnetic flux enclosed by the eddy currents, and L_{eddy} corresponds to the self-inductance of the eddy currents. The value of L_{eddy} can be approximately calculated using (2.1) by assuming that the eddy currents are two current filaments of width $\frac{w}{\alpha}$ with a separation of $\left(1 - \frac{1}{\alpha}\right)w$ (Fig. 3.22):

$$L_{eddy} = \frac{\mu_0}{\pi} l \cdot ln(\alpha - 1). \tag{3.33}$$

α can be assumed to be 5 for practical modeling. R_{eddy} then models the loss due to the eddy current. The weakness of such couple LR circuit is that magnitude of the trans-

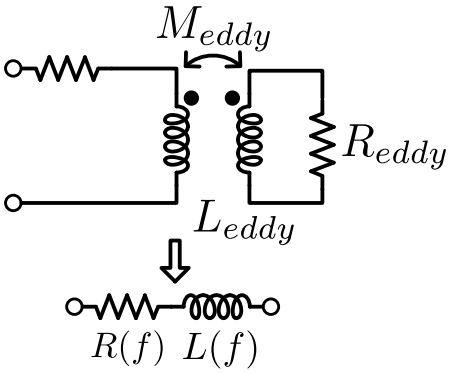

Figure 3.21: Coupled LR Circuit

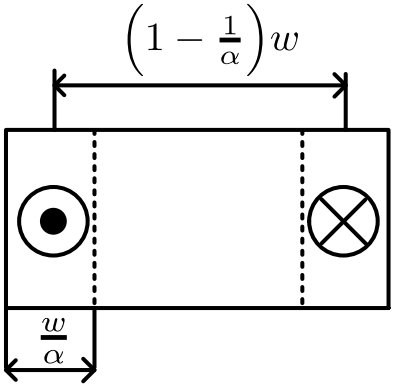

Figure 3.22: Illustration of Eddy Current in a Conductor

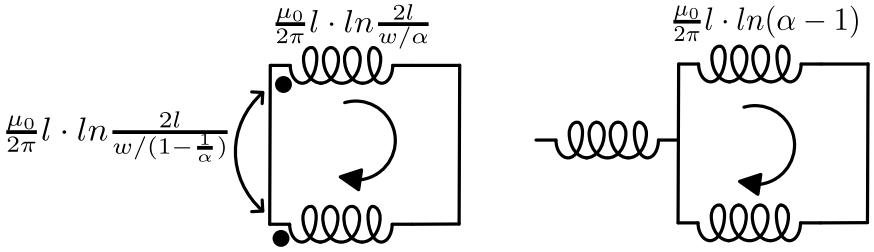

Figure 3.23: Equivalent Circuit to Calculate L_{eddy}

formed impedance $|Z_{in}|$ is not proportional to $\sqrt{f}$ at high frequency. In [15], the resistor R_{eddy} is changed to the same LR ladder in Fig. 3.18 to generate a $\sqrt{f}$ dependence on the proximity effect loss. At low frequency, the LR ladder on the load side behaves like a single resistor, so $|Z_{in}|$ is still proportional to f^2 as predicted by electromagnetic analysis.

The most accurate way to pick the $L's$ and $R's$ in the coupled LR ladder circuit is still curve fitting, but [15] proposed a simplified solution (Fig. 3.24). The eddy current within the conductor can be treated as a current loop circulating two halves of the conductor. If the LR ladder in Fig. 3.18 models the loss of the whole conductor, it can be divided into two parallel parts with all $L's$ and $R's$ multiplied by 2. $L_{eddy}/2$ is in series with two LR ladders, so that the circulating eddy current sees a self-inductance of L_{eddy}. $L_{eddy}/4$ is subtracted from L_{ext} of the original equivalent circuit so that the

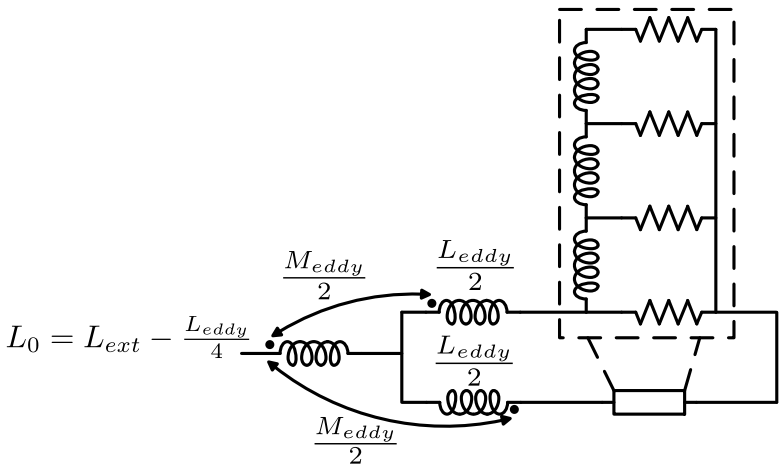

Figure 3.24: The Complete Circuit Modeling the Skin and the Proximity Effect

original LR ladder is intact in absence of the proximity effect. The emf induced by the flux enclosed by the conductor is modeled by a differential mutual inductance $M_{eddy}/2$ coupling L_0 and $L'_{eddy}s$, because the proximity effect is an odd mode loss. The results of case studies in Ch. 5 show that this approximation is good enough for practical designs.

3.2 A simplified substrate model

The equivalent shunt sub-circuit for the silicon substrate is developed using simple reasoning (Fig. 3.25). The capacitor C_{ox} models the displacement current in the oxide layer between the top metal and the silicon substrate. Since the silicon substrate is semi-conducting, the **E** field will produce real current in the substrate, which is modeled by R_{si}. In addition, C_{si} is inserted in parallel with R_{si} to model the relaxation behavior of silicon. The relaxation time constant, which is should be equal to $R_{si}C_{si}$, is

$$\tau_{si} = \rho_{si}\varepsilon_{si}\varepsilon_0 = 0.1 \times 11.9 \times \varepsilon_0 \approx 10\ ps \Longleftrightarrow 15\ GHz. \tag{3.34}$$

(3.34) means that the silicon substrate behaves more like a resistor in typical CMOS RF frequency ($0.1\ GHz \sim 10\ GHz$). Beyond RF, the relaxation capacitance shunts the resistance, and C_{ox} in series with C_{si} allows a quasi-TEM mode transmission. In [6], Yue proposed the expressions for C_{ox}, R_{si} and C_{si} in terms of the inductor geometry

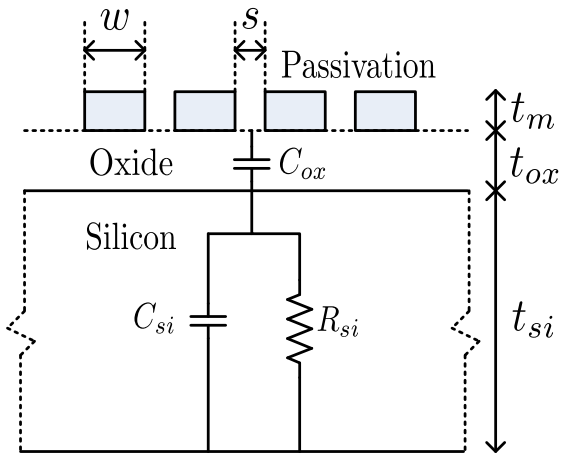

Figure 3.25: Cross Section of the Inductor

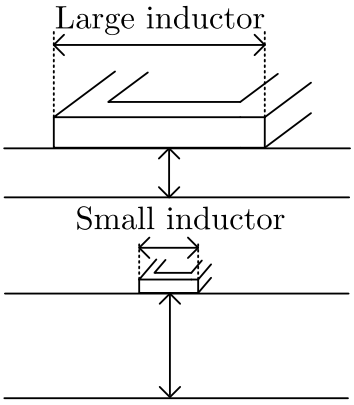

Figure 3.26: Aspect Ratios

based on the uniform parallel plate field model as follow

$$C_{ox} = \varepsilon_{ox}\varepsilon_0 \cdot \frac{A_{metal}}{t_{ox}}, \tag{3.35}$$

$$C_{si} = \varepsilon_{si}\varepsilon_0 \cdot \frac{A_{metal}}{t_{si}}, \tag{3.36}$$

and

$$R_{si} = \rho_{si} \cdot \frac{t_{si}}{A_{metal}}, \tag{3.37}$$

where A_{metal} is the total area of the metal traces. This model can easily be used by designers. However, a prerequisite of this model is that the lateral dimension of the metal area is much larger than the thickness of the substrate (Fig. 3.26). Such aspect ratio was probably prevalent in old designs 20 years ago, but as the operating frequency increases, L shrinks. In today's design, small single-turn or two-turn inductors are commonly seen, and the electric fields under those inductors are predominantly fringing fields .

To take the fringing fields into consideration, many researchers embrace the model of microstrip transmission line on Si-SiO_2 system, where the complete electrical fields in the substrate are captured [37]. Maxwell's equations are solved to obtain three basic modes of propagation and their corresponding per-unit-length equivalent circuit (Fig. 3.27). In simple words, dielectric quasi-TEM mode happens on highly resistive

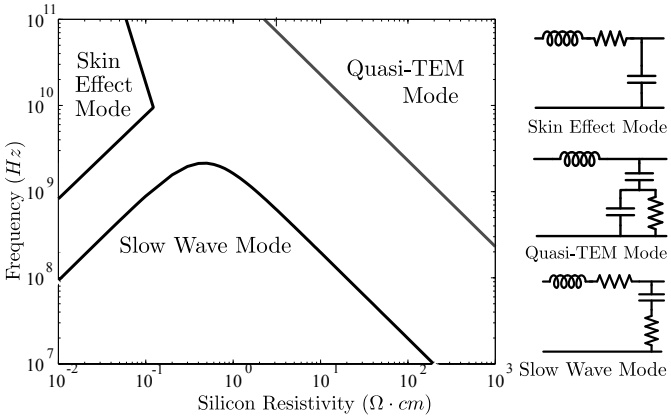

Figure 3.27: Three Modes of Operation and Equivalent Circuits [3]

silicon at very high frequency ($> 10\ GHz$). Skin effect mode corresponds to the effect of substrate eddy currents that was qualitatively described in papers on inductor modeling [38]. The per-unit-length equivalent circuit of the skin effect mode includes a frequency-dependent resistance and a frequency-dependent inductance, which model the loss and the image effect due to the lateral currents in the highly conductive substrate. This approach is equivalent to modeling the substrate eddy current under the inductor with a coupled RL loop (Fig. 3.21).

According to Fig. 3.27, typical RF circuits ($0.1\ GHz \sim 10\ GHz$) built on modern lightly doped silicon substrate ($10\Omega \cdot cm$) operate in the transition region between slow wave mode and quasi-TEM mode. Hence, it is no longer necessary to model the substrate eddy currents, which correspond to the skin effect mode. The per-unit-length equivalent circuits for slow wave mode and quasi-TEM mode prove our initial reasoning, as in the silicon substrate can be modeled as a RC network. Based on the analysis in [37], the per-unit-length circuit parameters are

$$C_{ox} = \frac{\varepsilon_0 \varepsilon_{eff}(\varepsilon_{ox}, t_{ox})}{F(t_{ox}, w)} \tag{3.38}$$

$$C_{si} = \frac{\varepsilon_0 \varepsilon_{eff}(\varepsilon_{si}, t_{si})}{F(t_{si}, w)} \tag{3.39}$$

$$R_{si} = \frac{2F(t_{si}, w)\rho_{si}}{1 + \left[1 + \left(\frac{10t_{si}}{w}\right)^{-1/2}\right]} \tag{3.40}$$

where F and ε_{eff} are

$$F(t,w) = \begin{cases} \dfrac{1}{2\pi} ln\left(\dfrac{8t}{w} + \dfrac{w}{4t}\right) & \text{if } \dfrac{t}{w} > 1, \\ \left[\dfrac{w}{t} + 2.42 - \dfrac{0.44t}{w} + \left(1 - \dfrac{t}{w}\right)^6\right]^{-1} & \text{if } \dfrac{t}{w} < 1, \end{cases} \tag{3.41}$$

$$\varepsilon_{eff}(\varepsilon,t) = \frac{\varepsilon+1}{2} + \frac{\varepsilon-1}{2\sqrt{1+10t/w}}, \tag{3.42}$$

which are widely used in existing inductor models. However, the model in [37] is for a *single straight* transmission line on silicon, which is no longer a valid situation for spirals. As shown in Fig. 3.28, the **E** fields that come from the sandwiched turns are more confined than those from a single transmission line. If one calculated the circuit parameters assuming the inductor were a straight trace of the same length, he would have overestimated the actual substrate conductance. This error does not appear as an obvious one, because shunt loss and capacitance are typically overwhelmed by the series loss and inter-winding capacitance on lightly doped silicon.

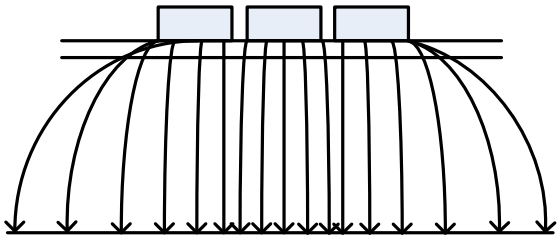

Figure 3.28: **E** Fields of Multiple Conductors over Silicon

To resolve the aforementioned problem, [15] added another fitting parameter depending on the coupling coefficient between adjacent segments. Specifically, the effective depth and permittivity of the substrate under the sandwiched turns are adjusted back to the values in absence of the fringing fields. The method is creative and accurate, but it is still too complicated for a simple design-oriented analysis.

As shown in Fig. 3.29, the concept of spreading resistance is borrowed from the design of point-contact rectifiers [39]. When a circular point contact with a radius r

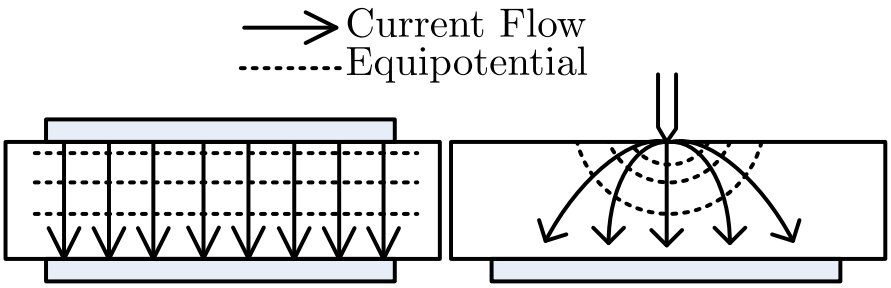

Figure 3.29: Large Contact (left) and Point Contact (right)

is placed on a semi-infinite substrate whose thickness $t_{si} \gg 2r$, the total resistance to ground is

$$R = \frac{\rho_{si}}{4r}, \tag{3.43}$$

Notice that the resistance increases inversely as the radius of the contact, not inversely as the area, and the spreading resistance effect is felt in full [39]. But when $t_{si} \ll 2r$, resistance to ground is inversely proportional to the area, and the parallel-plate resistance is predominant. In [40], field equations were solved for a universal equation of resistance from a contact to ground for all aspect ratios of r to t_{si} as follow

$$R = \frac{\rho_{si}}{2\pi r} \tan^{-1}\left(\frac{k(t_{si})t_{si}}{r}\right), \tag{3.44}$$

where

$$k(t_{si}) = 1 + \frac{1}{1 + t_{si}/r}. \tag{3.45}$$

A square contact can simply be approximated as a disk contact with the same area.

Now, what if the contact is a ring, like the shape of an inductor, instead of a solid disk? This problem has been studied by measurements in [41, 42] to predict the thermal spreading resistance of a ring-geometry diode. Due to the well-known analogy between thermal laws and electrical laws, the results of the study can be direcly used. Consider a disk of radius r, which feels spreading resistance fully. The total resistance of this contact will increase if a hole of radius b was cut in it. Fig. 3.30 shows the measured change in resistance with respect to the relative size of the hole. Interestingly, the

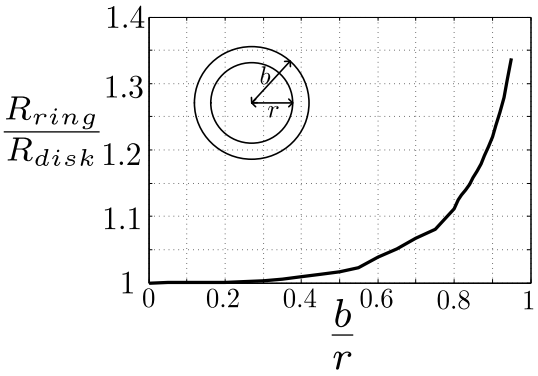

Figure 3.30: Spreading Resistance of a Ring Normalized to that of a Disk

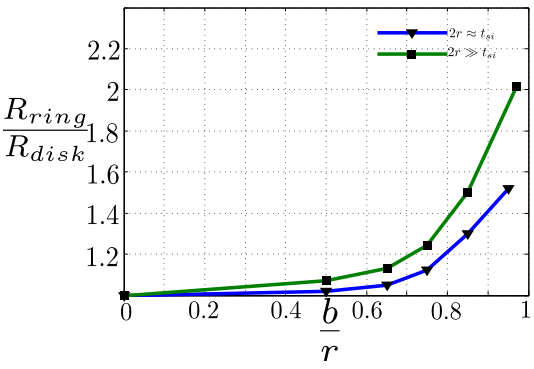

Figure 3.31: Generalization of Fig. 3.30

resistance is only increased by less than 20% if the radius of the hole is less than 90% of the radius of the disk.

Can this expriment be generalized to cover the situation where the dimension of the original disk is already comparable or much larger than the substrate thickness? A simple simulation is setup in ADS Momentum to measure the total impedance from a ring of metal to ground with customized substrate thickness. The simulated changes in the total resistance to ground for $2r \approx t_{si}$ and $2r \gg t_{si}$ are shown in Fig. 3.31

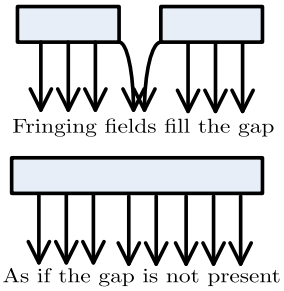

Figure 3.32: **E** Fields of Closely Coupled Conductors

The above three curves in Fig. 3.30 and Fig. 3.31 imply that the total spreading resistance of a ring will not be drastically different from that of a disk with the same outer dimension. Note that this ratio is typical for normal spiral inductors, if $r_{in}/r_{out} <$

0.8. Also since the inter-turn spacing is usually smaller than the trace width, the **E** field lines originating from the traces will converge in the substrate, as if the inter-turn space is not present (Fig. 3.32). Then, the total substrate resistance R_{si} can be estimated simply from the outer and the inner radius of the inductor. Once R_{si} is determined, C_{si} will just be τ_{si}/R_{si}.

3.3 A Summary of the Distributed Capacitance Model

The distributed capacitance captures the electric energy stored between the windings, which is critical in determining the self-resonant frequency of an inductor. The circuit theories related to Q and self-resonant frequency will be discussed later in Ch. 4. The existing methods of calculating the distributed capacitance are proven to be effective by numerous case studies during the research, some of which will be shown in Ch. 5. This section covers the process of lumping the distributed capacitances, the models of the physical capacitances, and the distributed effects of the substrate network.

The analysis of the stored electric energy between windings starts from determining the voltage profile of an inductor. If all the spiral is stretched out to a single straight metal bar, the voltage distribution across bar will always be linear, when it is driven from both ends. However, winding the bar into a spiral introduces varying mutual coupling inductances between non-adjacent turns, so the voltage drop across the spiral is not necessarily linear. In [43], the author analyzed the voltage profiles of typical unsymmetrical inductors. The results show that as long as the traces are compactly wound, voltage distribution across the spiral will be very close to linear. This approximation can be generalized to model the voltage distribution of symmetrical inductors, since the coupling coefficients between turns in symmetrical inductors are similar to those in unsymmetrical ones.

In light of the linear voltage profile, an N-turn symmetrical spiral can be segmented into 2N half arcs Fig. 3.33. The total voltage drop across each segment in proportional

to the length of that segment. For more simplification, the voltage of each half arc V_k can be equalized to the average of the voltages on its two ends:

$$V_{k\ begin} = V_0\Big[1 - \sum_{i=1}^{k-1} \frac{l_i}{l_{tt}}\Big] \tag{3.46}$$

$$V_{k\ end} = V_0\Big[1 - \sum_{i=1}^{k} \frac{l_i}{l_{tt}}\Big] \tag{3.47}$$

$$V_k = \frac{1}{2}\Big[V_{k\ begin} + V_{k\ end}\Big] = (-1)^{k-1} \cdot \frac{1}{2} V_0\Big[2 - \sum_{i=1}^{k-1} \frac{l_i}{l_{tt}} - \sum_{i=1}^{k} \frac{l_i}{l_{tt}}\Big], \tag{3.48}$$

where l_{tt} is the total length of the half arcs on one side, and l_i is the length of the i^{th} arc [44].

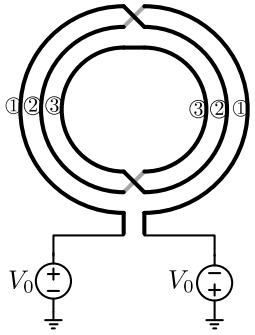

Figure 3.33: Segments of a Symmetrical Inductor

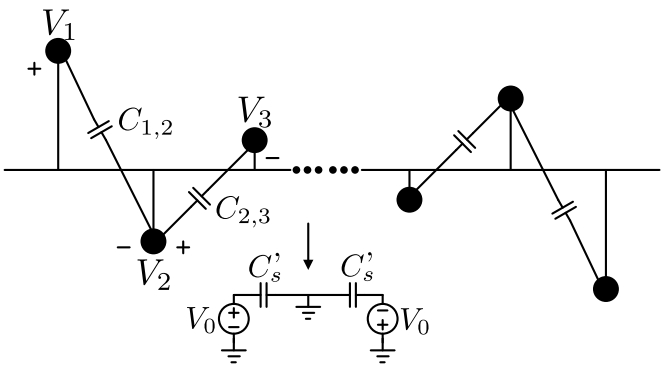

Figure 3.34: Voltage Profile

The voltage profile of the inductor, driven differentially, is shown in Fig. 3.34 where $C_{k,k+1}$ is the physical inter-wire capacitance between each adjacent segments and can be calculated using

$$C_{k,k+1} = C_{couple} \cdot \frac{1}{2}\big(l_k + l_{k+1}\big). \tag{3.49}$$

C_{couple} is the per-unit-length inter-wire capacitance to be introduced later. The capacitor C_s' needs to store the same amount of energy as all the capacitors on the voltage profile do:

$$\sum_{k=1}^{N-1} \frac{1}{2} C_{k,k+1} \cdot \big(V_k - V_{k+1}\big)^2 = \frac{1}{2} C_s' V_0^2. \tag{3.50}$$

Once, C_s' is determined, C_s will then be $1/2\ C_s'$.

The modeling of C_{couple} is a well-studied topic in digital integrated circuits. Some classical models include [45, 46], nearly all of which used curving fitting based on measurements. In this work, a newly-published physics-based analytical model of inter-wire capacitance is adopted [47]. The model includes the effects of shielding and sharing of electric field lines in multi-electrode cases. Details of the derivation are well explained in [47], so a brief summary of the model relevant to on-chip inductors is presented here.

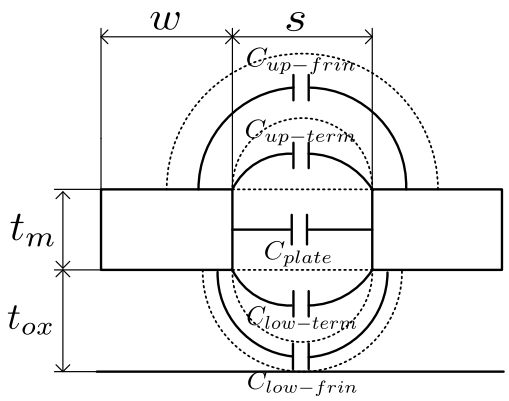

Figure 3.35: Inter-wire Capacitances

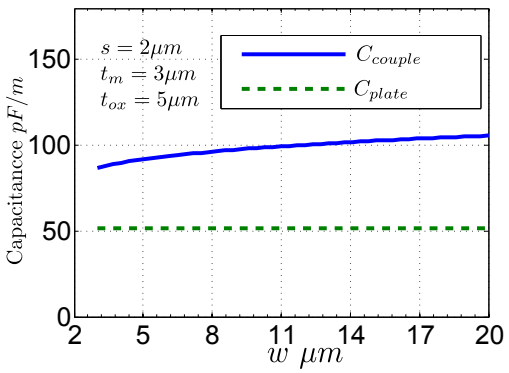

Figure 3.36: C_{couple} vs w

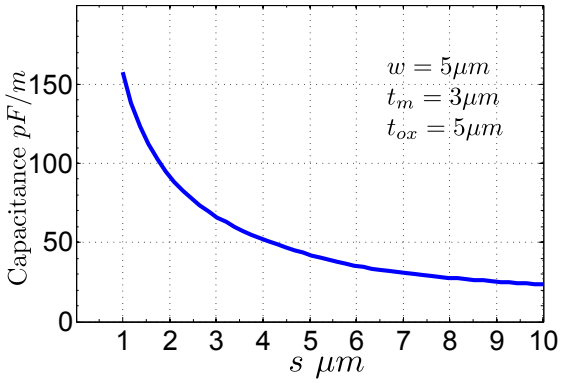

Figure 3.37: C_{couple} vs s

Fig. 3.35 concludes the models of the three types of inter-wire capacitances, parallel plate capacitance (C_{plate}), terminal capacitance (C_{term}), and fringing capacitance (C_{frin}). Their values are adjusted from the three canonical cases described in [47] to

address the shielding effects and multi-electrode effects. Each capacitance can be calculated using (10), (12), (14) and Table II in [47]. C_{couple} is the sum of all the individual capacitances listed in Fig. 3.35.

Fig. 3.36 demonstrates the dependence of C_{couple} on w, when t_m and s are fixed. Note that C_{couple} stays relatively constant with varying metal width, and it is nearly twice as large as the capacitance calculated from pure parallel plate capacitance equation $\varepsilon t_m/s$. Although that ratio will increase with increasing s and t_{ox}, a ratio of 2 can still be used to guess the inter-winding capacitance, because well-designed inductors in modern CMOS processes are typically compactly wound and have similar $t'_m s$ and $t'_{ox} s$ as those listed in Fig. 3.36.

Fig. 3.37 indicates that C_{couple} depends heavily on the spacing between turns. Hence, a design implication is that single turn inductors or loosely-wound multi-turn inductors are usually designed in applications where the self-resonant frequency must be high. For example[30], discrete RF chokes employ spaced windings to limit the distributed capacitance.

Besides the effect of the distributed inter-winding capacitance, the modeling of the substrate parasitics also needs to include the distributed effect. Previously in Ch. 3.2, C_{ox} is calculated as the parallel-plate capacitance between a solid ring and the substrate, as if all the spacings are filled by metal. The validity of this assumption can be tested using the model of C_{bottom} in [47]. Fig. 3.38 shows the cross sectional diagram of the bottom capacitances, which can be calculated by (19), (20), (21) and Table III in [47].

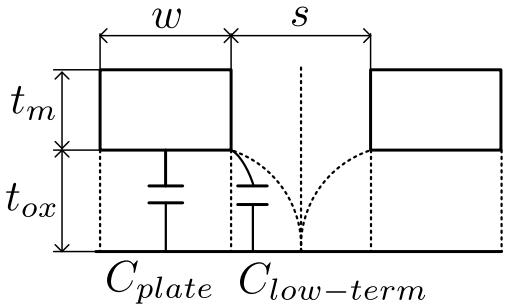

Figure 3.38: Oxide Capacitances

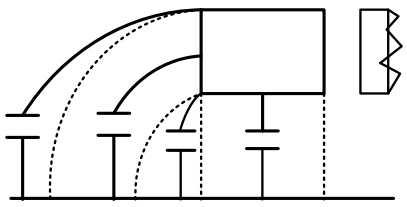

Figure 3.39: Unshielded Outermost Turn

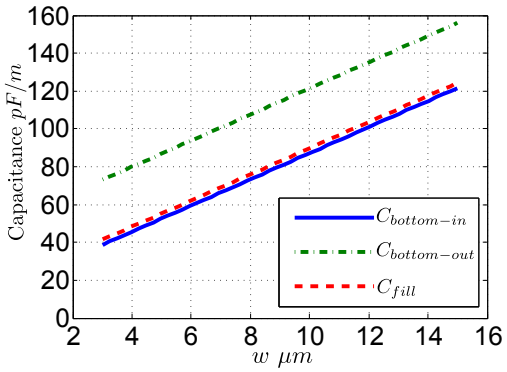

Figure 3.40: Comparison between Oxide Capacitances

C_{bottom} can then be calculated by

$$C_{bottom-in} = C_{plate} + 2C_{low-term}. \tag{3.51}$$

For a spiral inductor, the outermost sides have larger C_{bottom}, because the field lines there are not shielded by adjacent turns (Fig. 3.39). Hence, C_{frin} and C_{term} should return to the canonical cases introduced in [47]:

$$C_{bottom-out} = C_{plate} + C_{low-term} + \varepsilon\frac{6}{\pi} + \varepsilon\frac{4}{\pi}ln\left(1+\frac{t_m}{t_{ox}}\right). \tag{3.52}$$

Fig. 3.40 compares $C_{bottom-out}$, $C_{bottom-in}$, and the approximated parallel plate capacitance with the spacings filled (C_{fill}). Note that $C_{bottom-in}$ is well approximated by C_{fill}, which proves the validity of the assumption made in Ch. 3.2 about C_{ox}. From a designer's perspective, the analytical models of $C_{bottom-out}$ and $C_{bottom-in}$ can be used with the help of a computer, but an approximated C_{fill} (or C_{ox}) is still applicable for initial estimation.

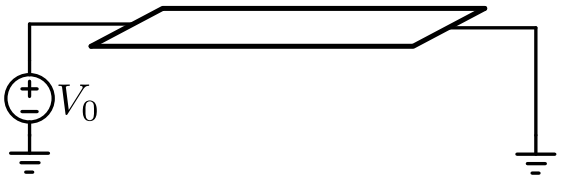

Figure 3.41: Metal Bar on a Ground Plane

The process of modeling the distributed substrate parasitics with circuits is similar to that used to model the inter-wire capacitance. Consider a solid metal bar placed on a ground plane, with one port driven to V_0 and the other port grounded (Fig. 3.41). C_{pu} is the capacitance to ground per unit length. Since the voltage distribution is linear, the total energy stored is

$$\frac{1}{2}\int_0^{l_{tt}} C_{pu}V_0\frac{x}{l_{tt}}dx \;=\; \frac{1}{2}\cdot\frac{1}{3}\,C_{pu}\cdot l_{tt}V_0^2, \tag{3.53}$$

which means that the effective capacitance is $1/3\;C_{pu}l_{tt}$. When both ports are driven by the same voltage, the total capacitance is simply $C_{pu}l_{tt}$. If the equivalent model is a 1-π model (Fig. 3.42), only one of the two situations can be modeled correctly. However, a 2-π model satisfies both conditions simultaneously (Fig. 3.43).

$$\begin{cases} \frac{1}{2}C_1V_0^2+\frac{1}{2}C_2\frac{1}{4}V_0^2=\frac{1}{2}\cdot\frac{1}{3}\cdot C_{total}V_0^2 \\ C_1+C_2=C_{total} \end{cases} \tag{3.54}$$

$$\Longrightarrow \begin{cases} C_1=\frac{1}{6}\,C_{total} \\ C_2=\frac{2}{3}\,C_{total} \end{cases} \tag{3.55}$$

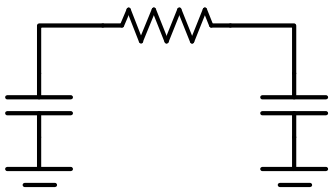

Figure 3.42: 1-π Circuit

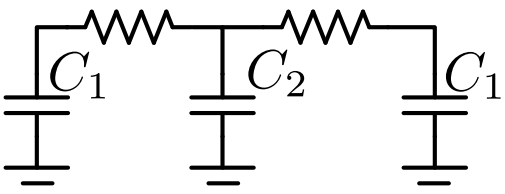

Figure 3.43: 2-π Circuit

As discussed before, in real inductors, C_{pu} of the outermost turn is different from that of the other turns, so the distribution factor in (3.55) is just an approximation to the reality. In Ch. 5, examples will prove that the approximated distribution factor can be used for all practical purposes.

3.4 The Complete Equivalent Circuit

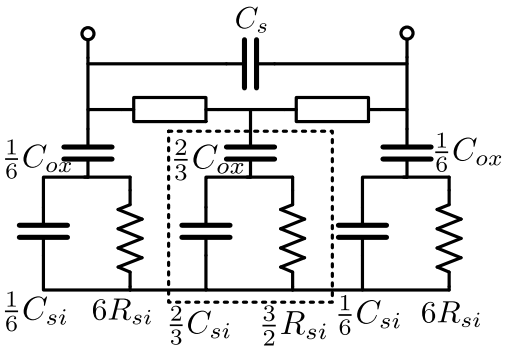

Figure 3.44: 2-π Equivalent Circuit

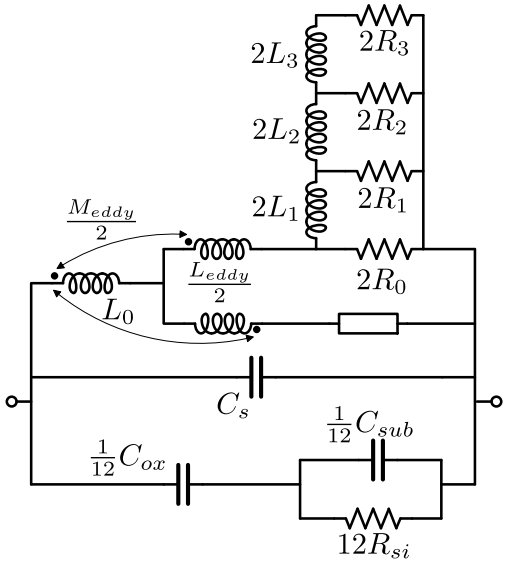

Figure 3.45: Complete 1-port Equivalent Circuit

Fig. 3.44 shows the 2-π equivalent circuit of the inductor. When driven differentially, the branch enclosed in the dashed box is nulled, because the center-tap node is ac grounded. The equivalent circuit can then be re-drawn into a 1-port circuit shown in Fig. 3.45. All the $R's$ and $L's$ in the ladder can be calculated using the methods described in Ch. 3.1. L_{eddy} is calculated using (3.33). L_{dc} comes from (2.3). Then,

$$L_0 = L_{dc} - \frac{L_{eddy}}{4} - L_{int}, \tag{3.56}$$

where L_{int} is calculated by (3.18). M_{eddy} models the total enclosed even mode flux by all turns of the inductor.

$$\frac{M_{eddy}}{1A} = M_{eddy} = \sum_i \mu_0 H_i \times w \times l_i, \tag{3.57}$$

where l_i is the length of each turn, H_i is the even mode external field in each turn calculated based on (2.6).

C_s, C_{ox}, C_{si}, and R_{si} are calculated using the methods introduced in Ch. 3.2 and Ch. 3.3.

CHAPTER 4

Definitions of the Quality Factor

4.1 Why Discussing Q?

The quality factor (Q) is a key figure of merit judging the performance of an inductor and is also the objective in the optimization process. A correct definition of Q properly connects the equivalent circuit with the optimization process. A low-entropy expression of Q in terms of circuit parameters provides insights to circuit engineers during the initial design estimation. The vagueness of and the conflicts among different definitions of Q have already been recognized by previous works, such as [48, 49]. However, the majority of the literature on inductor modeling put their complete efforts on the equivalent circuits and assumed that the definition of Q was well-understood. The lack of discussion on Q causes confusions when engineers use the equivalent models. We believe that a useful inductor model should contain a clear discussion on different definitions of Q and corresponding explanations of their usages. This chapter summarizes some insightful studies on the definitions of Q and resonant frequency. Some design-oriented expressions for different definitions of Q are also proposed.

4.2 Connection between Impedance and Stored Energy

Before the discussion of Q, it is necessary to revise the connection between the driving point impedance and the stored energy of a network. Given an arbitrary LTI network with two terminals driven by a current source I, one can prove using the Uniqueness

Theorem [50] that

$$Z_{in} = R + jX = \frac{2P}{|I|^2} + \frac{4j\omega(W_m - W_e)}{|I|^2}, \tag{4.1}$$

where W_e is the mean electric energy stored, and W_m is the mean magnetic energy stored. P is the total power dissipation at the driving point. Since the total stored energy is constant and is oscillating between electric energy and magnetic energy. The total energy in the system is $W = W_e + W_m$.

4.3 Origination of Q from the 2nd-Order Circuit

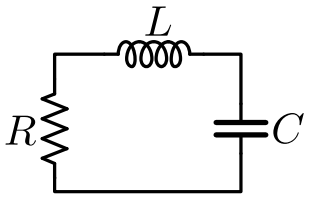

Figure 4.1: Series LCR Circuit

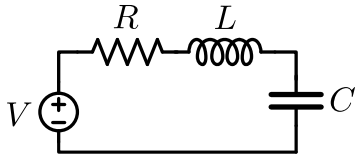

Figure 4.2: Voltage Stimulus Inserted into Series LCR Circuit

In basic circuit theory, Q is used to characterize the series (or parallel) LCR circuit (Fig. 4.1). Excited without changing the circuit topology, the series (or parallel) LCR circuit has two poles in its network functions. Writing the denominator of the network function into the canonical form

$$D(s) = 1 + \frac{s}{\omega_0 Q} + \frac{s^2}{{\omega_0}^2} = 1 + s\frac{L}{R} + s^2 LC \tag{4.2}$$

reveals the quality factor $Q = \frac{1/R}{\sqrt{C/L}}$and the natural frequency $\omega_0 = \frac{1}{\sqrt{LC}}$ of the 2nd-order system. This Q can written as $\frac{\omega_0 L}{R}$ and is only defined at the natural frequency. Since the natural frequency of the series LCR circuit can be tuned to any frequency by varying C, Q can be defined as a function of frequency. Then,

$$Q = \frac{\omega L}{R}. \tag{4.3}$$

The definition of Q is consistent with the fundamental definition of Q in physics, which

is

$$Q_{fund} = \frac{total\ energy\ stored}{energy\ dissipated/rad}. \tag{4.4}$$

Q_{fund} can only be determined using (4.4) if all the energies stored and dissipation in the network can be calculated. This may not be easy for a complicated black box circuit. [50] proves that for a one port network, the driving point reactance and susceptance have properties as follow:

$$\frac{dX}{d\omega} = \frac{4W}{|I|^2} \tag{4.5}$$

$$\frac{dB}{d\omega} = \frac{4W}{|V|^2}, \tag{4.6}$$

where I and V are the driving point current and voltage stimuli. Using (4.4),

$$Q_{fund} = 2\pi f \frac{\frac{1}{4}|I|^2 \frac{dX}{d\omega}}{mean\ power\ dissipated} \tag{4.7}$$

$$= 2\pi f \frac{\frac{1}{4}|V|^2 \frac{dB}{d\omega}}{mean\ power\ dissipated}. \tag{4.8}$$

Since the average power dissipation $P = \frac{1}{2}|V|^2 G = \frac{1}{2}|I|^2 R$, (4.7) and (4.8) can be written as

$$Q_{fund} = \frac{\omega}{2R}\frac{dX}{d\omega} \tag{4.9}$$

$$= \frac{\omega}{2G}\frac{dB}{d\omega}. \tag{4.10}$$

(4.9) and (4.10) simplify the calculation of the Q_{fund} of a complex network, because the specific energies stored in $L's$ and $C's$ within the network are no longer needed. If the driving point impedance of a complex network is known, the stored energy can be derived by taking the derivative of the reactance or susceptance numerically.

It must be emphasized that Q_{fund} is defined at the resonant frequency. Otherwise, the value of Q_{fund} will be meaningless. For example, for a series LCR circuit (Fig. 4.2), $Q_{fund} = \frac{\omega L}{2R} + \frac{1}{2\omega RC}$, which is infinite at DC or infinite frequency. Only at $\omega = \frac{1}{\sqrt{LC}}$, $Q_{fund} = \frac{1/R}{\sqrt{C/L}}$, which is consistent with the Q defined for the second order system.

4.4 Resonant Frequency

Since Q_{fund} is defined at the resonant frequency, it is necessary to clarify the definition of the resonant frequency (ω_0). According to [30], there are three definitions of ω_0

1. ω_{01}: The natural frequency of 2nd-order circuit with all stimuli suppressed
2. ω_{02}: The frequency where the magnitude of the input impedance is maximum
3. ω_{03}: The frequency where the input impedance is purely real

The theoretical values of $\omega_0's$ defined by the three methods are not the same. However, for a high Q 2nd-order circuit, when $Q_{fund} > 10$ at ω_{01}, these three frequencies can be treated as identical for all practical purposes [30].

This approximation of the resonant frequency can be generalized to higher order networks. For circuits of order larger than 2, ω_{01} fails, because one cannot put the denominator of the network function into the canonical form, like (4.2) and extract ω_0. However, if the Q of the system is assumed to be high (> 10), then ω_{03} can be measured simply from the input impedance of the network. With ω_{03}, one can calculate Q_{fund} using (4.9). If the calculated Q_{fund} agrees with the assumption (> 10), this Q can be used as a figure of merit for the network. On modern RF CMOS processes, resonators built for low-phase-noise oscillators typically have Q larger than 10, which allows the use of this method.

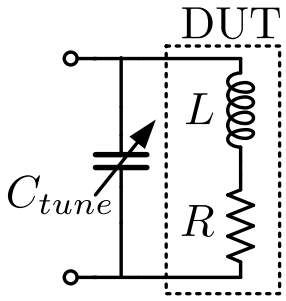

Figure 4.3: DUT at Low Frequency

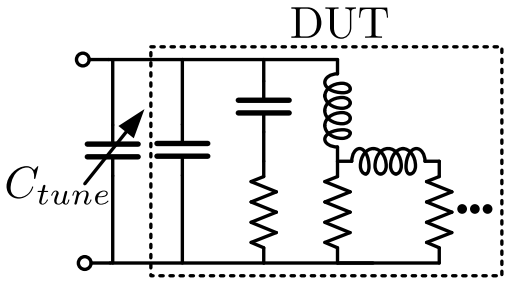

Figure 4.4: DUT at High Frequency

When the definition of ω_0 is known, Q_{fund} can be found as a function of frequency by tuning an unknown circuit to resonance at any frequency [51]. For an inductor, at low frequency when Q is low, all capacitive parasitics are not present, and the equivalent circuit with the tuning capacitor is shown in Fig. 4.3. Q_{fund} for this simple 2nd-order circuit is simply $\frac{\omega L}{R}$. At higher frequency, the amount of the extra capacitance needed to tune the inductor to resonance is less than $\frac{1}{\omega^2 L}$ (Fig. 4.4). The input impedance needs to be tuned to purely real, because the circuit is no longer 2nd-order. At the self-resonant frequency, no extra capacitance is needed to tune the input impedance to real. Thus, the fundamental definition of Q for inductors is only meaningful from DC to the self-resonant frequency, and there is inconsistency between tuning to resonance at low frequency and doing so at high frequency.

4.5 Why do people use $Im(Z)/Re(Z)$?

The definition of $Q_{ind} = \frac{Im(Z)}{Re(Z)}$ originates from popular measurement instruments. For example, HP4323 [52] treats an inductor under test as a black box with a frequency dependent L_{eff} and a frequency dependent R_{ac}. The equipment contains a self-regulating voltage injection that forces the voltage of the series tuning capacitor to be proportional to Q_{ind}. Other advanced measurements instruments like an LCR meter also measures the effective inductance $\frac{Im(Z)}{\omega}$ and effective resistance $Re(Z)$ of the inductor. According to the universal curve of high-Q parallel resonator in [30], when an inductor is approaching self-resonance, its effective inductance rises significantly and then decay rapidly to 0. When the inductor is used in parallel resonance, the change in the effective inductance does not affect the performance of the circuit, since a parallel capacitor can always be tuned accordingly such that the external capacitor and the distributed capacitor of the inductor form a resonator at the frequency of interest. However, when the inductor is used in series LCR circuit or ladder filters, the change in the effective inductance of the inductor will affect the circuit design, because L_{eff} is no longer its DC

value at high frequency. Four reasons explain why most people use Q_{ind} at a particular frequency of interest as the objective function for optimization.

1. Unlike Q_{fund}, Q_{ind} has consistent definition from DC up to the self resonant frequency.

2. Calculating Q_{ind} directly from the impedance without tuning or taking derivative is very simple, which minimizes computation complexity.

3. Q_{ind} clearly indicates the self-resonant frequency where the inductor no longer looks like an inductor from the input port.

4. In most cases, maximum Q_{ind} occurs at $1/3 \sim 1/2$ the self-resonant frequency where the effective inductance has not risen significantly.

Note that Q_{ind} is meaningless for the calculation of Q_{fund} for specific applications, because (4.1) implies that

$$Q_{ind} = \frac{2 \times (W_m - W_e)}{energy\ dissipated/rad}, \tag{4.11}$$

which is completely different from Q_{fund}. Once an inductor is put into the circuit, Q_{fund} of the resulting circuit needs to be calculated properly using the methods described in Ch. 4.3 and Ch. 4.4.

In order to illustrate the difference between Q_{ind} and Q_{fund}, a simple equivalent circuit for an inductor (Fig. 4.5) is taken from [53]. Due to the inconsistency of the resonant frequency discussed in Ch. 4.4, Q_{fund} is calculated from $600MHz$ instead of DC. Fig. 4.6 shows the comparison between Q_{fund} and Q_{ind}.

4.6 Design-Oriented Expression of Q_{ind}

A design-oriented expression of Q_{ind} for the equivalent circuit in Fig. 4.7 is improved from the expression proposed in [53] to account for the effect of self-resonance. In

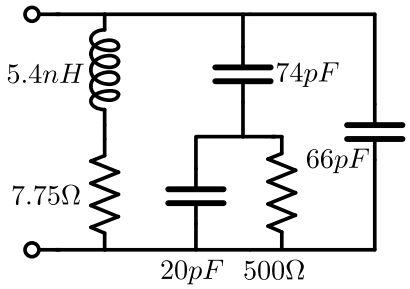

Figure 4.5: A Simple Equivalent Circuit

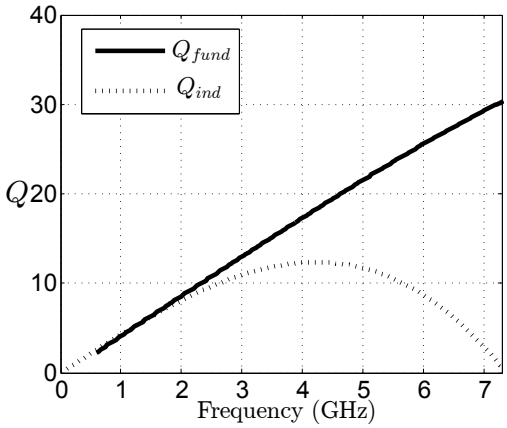

Figure 4.6: Q_{fund} and Q_{ind} of the Circuit in Fig. 4.5

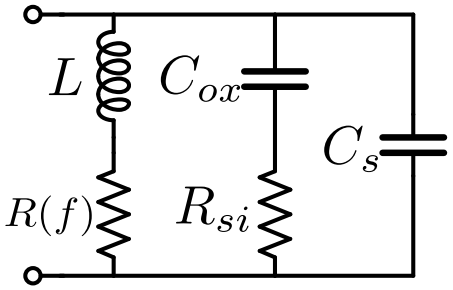

Figure 4.7: Simplified Equivalent Circuit

Fig. 4.7 C_{si} is ignored for simplicity.

$$Q \approx \frac{\omega L}{\underbrace{R(f)}_{series\ loss} + \underbrace{\frac{(\omega^2 L C_{ox})^2 R_{si}}{1+(\omega R_{si} C_{ox})^2}}_{substrate\ loss}} \underbrace{\left(1 - \frac{\omega^2 L(C_{ox}+C_s)}{1+(\omega R_{si} C_{ox})^2}\right)}_{self\ resonance} \tag{4.12}$$

4.7 Design-Oriented Expression of Q_{fund} in High Q Case

If $\frac{\omega L}{R(f)}$ in Fig. 4.7 is large (≥ 10), (4.13) can be used to approximate Q_{fund}.

$$Q_{fund} \approx \left[\frac{1}{\omega L} \cdot \left(1 + \frac{1}{(\omega R_{si} C_{ox})^2}\right) \cdot R_{si}\right] \Big|\Big| \frac{\omega L}{R(f)}. \tag{4.13}$$

CHAPTER 5

Case Studies and Optimization

5.1 Case I: A Commercial Inductor Supplied by A Company

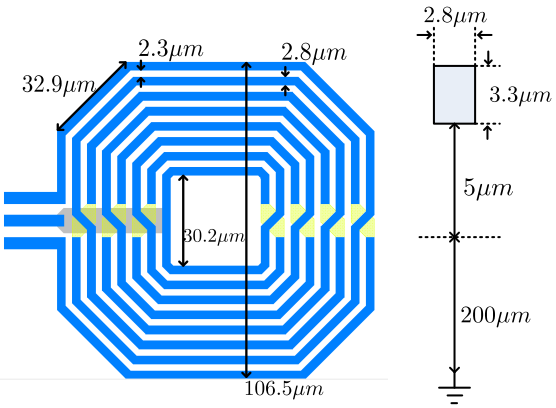

Figure 5.1: Case I Inductor Geometry

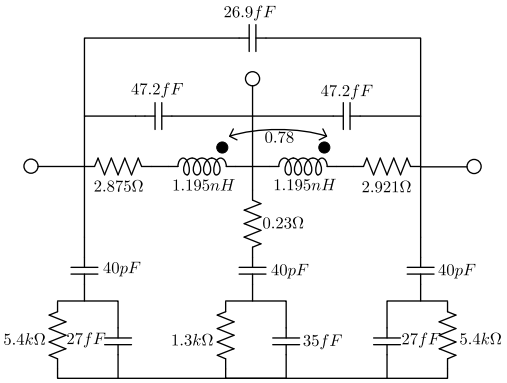

Figure 5.2: Case I Extracted Narrow Band Equivalent Circuit

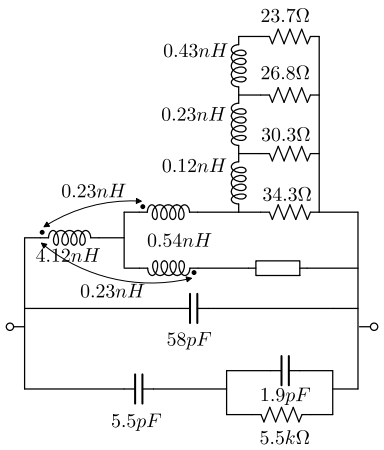

Figure 5.3: Case I Physical Equivalent Circuit

Fig. 5.1 shows an 8-turn symmetrical inductor designed recently in TSMC 65nm Process. The inductor is designed to operate at $5.5GHz$. The supplier also provides the simulated 3-port S-parameters and an extracted equivalent circuit at the frequency of operation (Fig. 5.2). Table 5.1 includes the estimated technology parameters.

Table 5.1: Estimated TSMC 65nm Technology Parameters

Name	Symbol	Value
M8 Sheet Resistance	$R_{\square}$	0.005Ω
M8 Thickness	t_m	$3.3\mu m$
Oxide Relative Permittivity	ε_{ox}	3.9
Oxide Thickness	t_{ox}	$5\mu m$
Substrate Relative Permittivity	ε_{si}	11.9
Substrate Thickness	t_{si}	$200\mu m$
Substrate Resistivity	ρ_{si}	$10\Omega \cdot cm$

Fig. 5.3 shows the physical equivalent circuit, whose components are all calculated based on the methods described in Ch. 3. ADS simulations are performed on the provided S-parameters, the extract equivalent circuit, and the physical equivalent circuit. All simulations assume that the inductor is operating in differential mode, so the input port is defined by the two signal terminals of the two ends of the inductor. The center tap port is left open during simulation.

Fig. 5.4 shows the calculated $Q_{ind} = \frac{Im(Z_{in})}{Re(Z_{in})}$ of the S-parameter black box, the extracted equivalent circuit, and the proposed physical equivalent circuit. It can be shown that Q_{ind} of the extracted equivalent circuit only agrees with that of the S-parameter black box at the frequency of operation ($5.5GHz$). It can be guessed that minimizing the error on Q_{ind} at $5.5GHz$ is one of the targets of the extraction process. In contrast, Q_{ind} predicted by the physical equivalent circuit agrees with the measurement from DC up to the self-resonant frequency of the inductor.

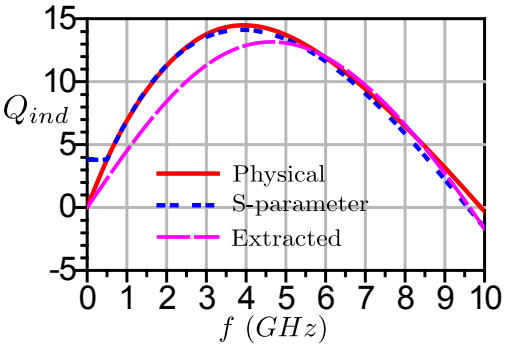

Figure 5.4: Q_{ind} of the Three Experiments

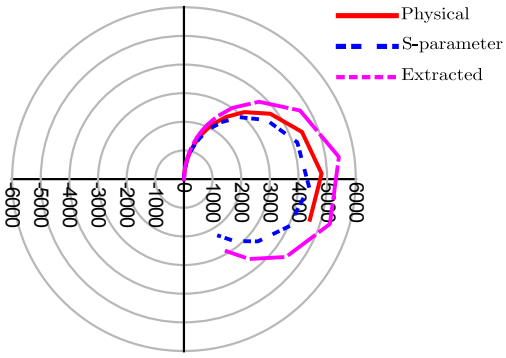

Figure 5.5: Z_{in} of the Three Experiments

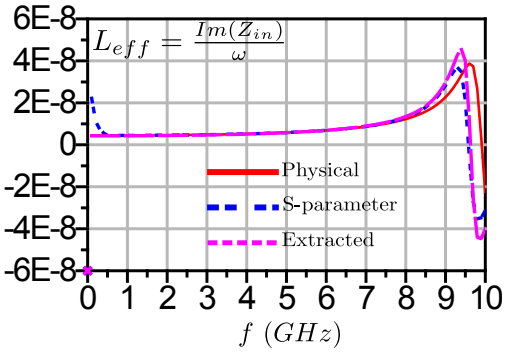

Figure 5.6: L_{eff} of the Three Experiments

Fig. 5.5 shows the input impedance of the inductor in differential mode. The physical equivalent circuit still gives a better prediction of the input impedance of the inductor. Note that at self resonance, the interpolation based on the S-parameters may not be accurate, so errors in magnitude and phase are tolerable.

Fig. 5.6 shows L_{eff} of the inductor over frequency. Despite the sensitive region near self resonance, both the extracted equivalent circuit and the physical equivalent circuit give good predictions on L_{eff}.

Since the proposed physical equivalent circuit models the skin effect loss and the proximity effect loss separately. It is possible to compare the effective series resistance under skin effect only and the one under both effects. C_s is also removed from the equivalent circuit to null the effect of resonance (Fig. 5.7). Fig. 5.8 shows that the

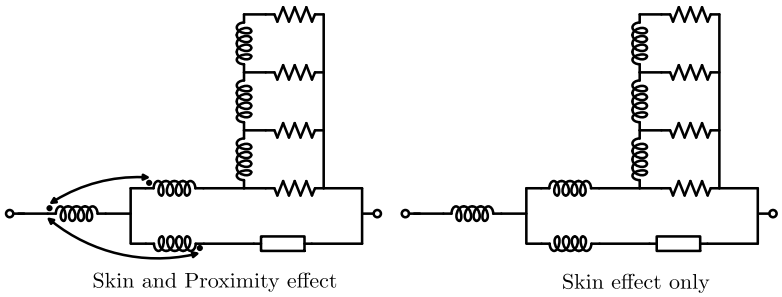

Figure 5.7: Subcircuits for Comparison

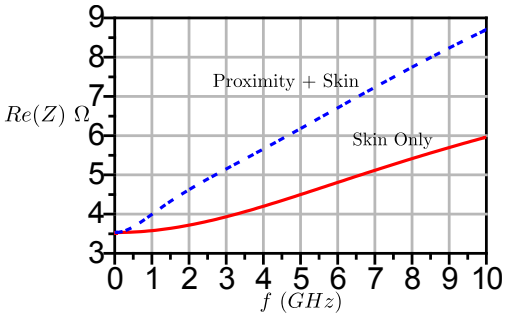

Figure 5.8: The Comparison between Losses with and without the Proximity Effect

proximity effect nearly doubles the series loss due to the skin effect only.

The physical equivalent circuit can be conveniently used to test whether an inductor is optimal at one frequency. In terms of optimization, the physical equivalent circuit substitutes the electromagnetic simulator in the optimization loop. The geometry of a inductor has only four variables,

1. Number of turns N,
2. Turn spacing s,
3. Turn Width w,
4. Inner diameter d_{in}.

Thus, if N is fixed, d_{in} can be calculated from the rest two variables w and s, for a given target L_{DC}. A surface of Q_{ind} at the frequency of operation can be calculated and plotted

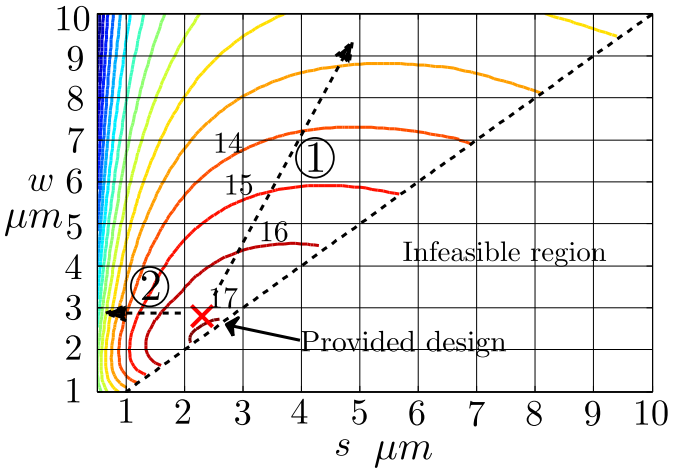

Figure 5.9: Contours of Q_{ind} at $5.5GHz$

as a function of w and s. Here, w is forced to be greater than s, which guarantees the accuracy of (2.3). Fig. 5.9 shows the contours of Q_{ind} at $5.5GHz$ for 8-turn inductors with different $w's$ and $s's$ but the same L_{DC} of $4.4nH$. The provided design is marked on the plot, and it is very close to the optimum. Small errors may be due to inaccuracy of the physical equivalent circuit. Following arrow ① means increasing the turn spacing and the turn width. Longer traces are needed to achieve the same L_{DC}, which means that R_{DC} is increased. Q_{ind} is then decreased. Following arrow ② leads to a more compact design, but the distributed capcacitance of the inductor is significantly increased, so that the self-resonant frequency and thus Q_{ind} are lower.

5.2 Case II: A Square Inductor from [1]

Case I demonstrates that the physical equivalent circuit can be used to predict whether an inductor is optimal at a frequency. However, the shape of the inductor in Case I is not regular, so it is hard to layout a sub-optimal inductor in the electromagnetic simulator with the same shape and verify the generality of the physical equivalent circuit. In other words, another test is needed to prove that the physical equivalent circuit can also model sub-optimal inductors. [1] presents a 5-turn square inductor with an L_{DC}

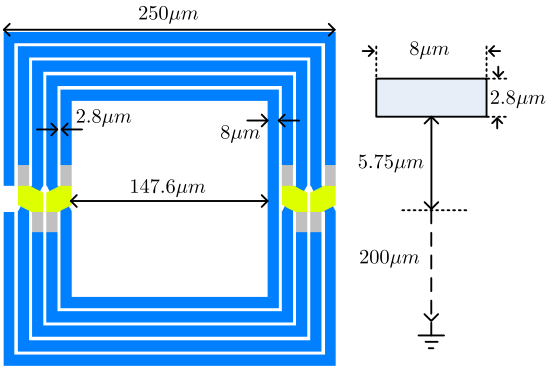

Figure 5.10: Optimal 5-turn Inductor at 2.5GHz

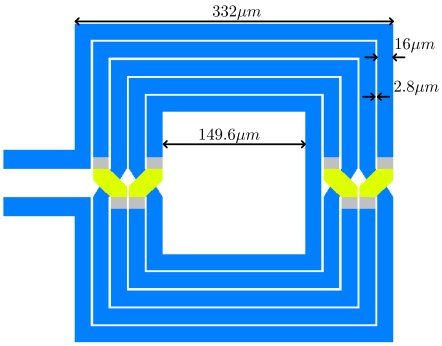

Figure 5.11: Sub-optimal 5-turn Inductor at 2.5GHz

of 8nH fabricated in SiGe BiCMOS process (Fig. 5.10). The technology parameters of the process are listed in Table 5.2.

Table 5.2: SiGe BiCMOS Technology Parameters

Name	Symbol	Value
Metal Resistivity	ρ_m	$3.1 \times 10^{-8} \Omega \cdot m$
Metal Thickness	t_m	$2.07 \mu m$
Oxide Relative Permittivity	ε_{ox}	3.9
Oxide Thickness	t_{ox}	$5.75 \mu m$
Substrate Relative Permittivity	ε_{si}	11.7
Substrate Thickness	t_{si}	$200 \mu m$
Substrate Resistivity	ρ_{si}	$15 \Omega \cdot cm$

The provided inductor is optimized at 2.5GHz. Based on the equivalent circuit, contours of Q_{ind} at 2.5GHz for different $w's$ and $s's$ are plotted in Fig. 5.12. The provided design is marked on the plot and falls inside the optimal contour of 10. Note that the optimum is quite flat, and choosing a tighter design with smaller w and s may save the chip area. In order to demonstrate the generality of the physical equivalent circuit, another sub-optimal inductor is synthesized to have the same s and a doubled w as

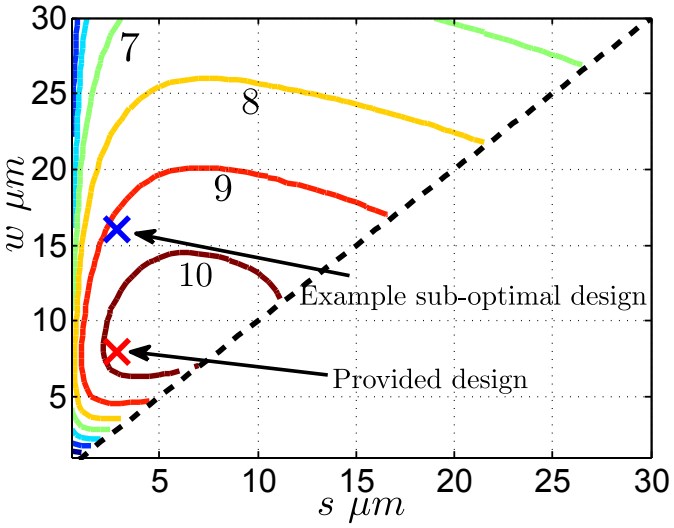

Figure 5.12: Contours of Q_{ind} at $2.5GHz$

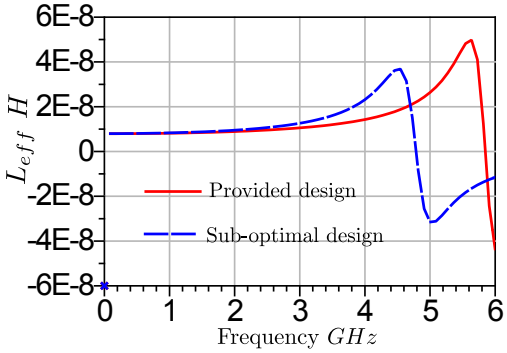

Figure 5.13: L_{eff} of the two Inductors

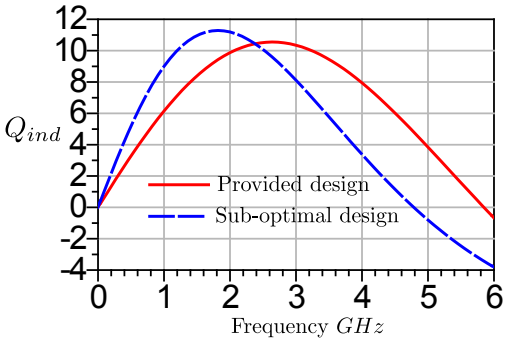

Figure 5.14: Q_{ind} of the two Inductors

the provided one. Fig. 5.11 shows geometry of the sub-optimal inductor. Electromagnetic simulation in ADS Momentum compares the performance of these two inductors. Fig. 5.13 proves that the two inductors have the same L_{DC}, so the comparison is fair. Fig. 5.14 shows that Q_{ind} of the sub-optimal inductor peaks at a lower frequency and rolls off to 9 at $2.5GHz$, which is also predicted by the contour of Q_{ind} based on the physical equivalent circuit.

The physical equivalent circuit is capable of explaining why the sub-optimal inductor has a lower Q_{ind} at $2.5GHz$. Firstly, the sub-optimal inductor has wider traces and thus longer total length of metal. As a result, the distributed capacitance and the sub-

strate parasitics are larger, which lowers the self-resonant frequency of the sub-optimal inductor. Also, wider traces enclose more common mode magnetic flux and leads to more serious proximity effects.

5.3 Case III: A Single Turn Inductor from [2]

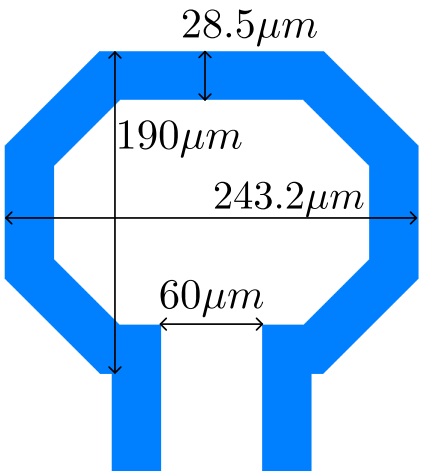

Figure 5.15: Case III Inductor Geometry

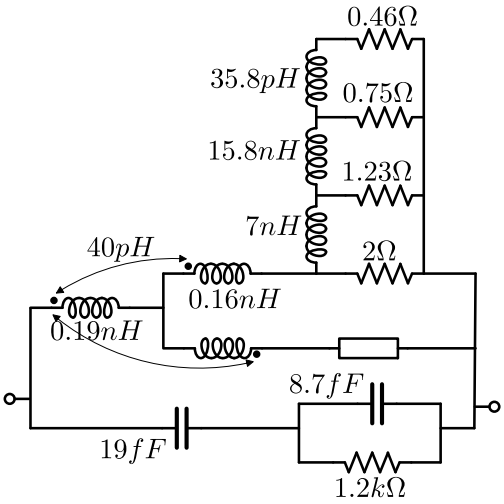

Figure 5.16: Case III Equivalent Circuit

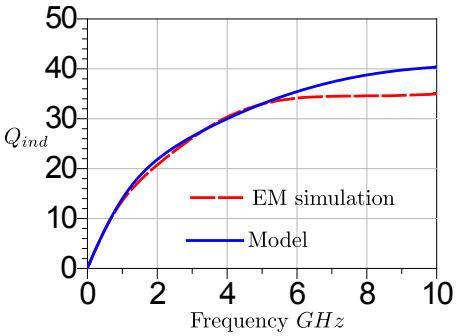

Figure 5.17: Q_{ind} of the Two Experiments

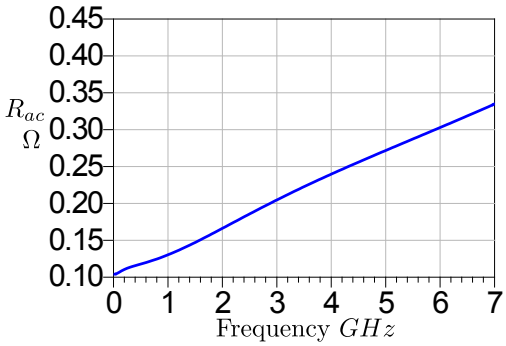

Figure 5.18: R_{ac} Calculated from the Ladder

Fig. 5.15 shows the geometry of a single-turn inductor used in [2] for a low-phase-noise oscillator. The inductor is built in TSMC 65nm process, so all relevant parameters

listed in Ch. 5.1 apply. The physical equivalent circuit in Fig. 5.16 does not include C_s, since the inductor has only one turn. Fig. 5.17 indicates that the equivalent circuit correctly predict Q_{ind} from DC to $6GHz$. At higher frequency, the lack of model for the small capacitance between two input terminals causes some discrepancies. According to Fig. 5.18, at $4GHz$, $R_{ac} = 0.24\Omega$ and Q_{fund} can be calculated using (4.13) as 22.8. At $5GHz$, $R_{ac} = 0.27\Omega$, and $Q_{fund} = 24.8$. These two results match the provided values of 22.5 and 25.5 at $4GHz$ and $5GHz$ respectively [2].

REFERENCES

[1] M. Danesh and J. Long, "Differentially driven symmetric microstrip inductors," *Microwave Theory and Techniques, IEEE Transactions on*, vol. 50, no. 1, pp. 332–341, Jan 2002.

[2] M. Tohidian, S. Mehr, and R. Bogdan, "Dual-core high-swing class-c oscillator with ultra-low phase noise," in *Radio Frequency Integrated Circuits Symposium (RFIC), 2013 IEEE*, June 2013, pp. 243–246.

[3] J. Long, Y. Zhao, Y. Jin, W. Wu, and M. Spirito, "Circuit technologies for mm-wave wireless systems on silicon," in *Custom Integrated Circuits Conference (CICC), 2011 IEEE*, Sept 2011, pp. 1–8.

[4] N. Nguyen and R. Meyer, "Si ic-compatible inductors and lc passive filters," *Solid-State Circuits, IEEE Journal of*, vol. 25, no. 4, pp. 1028–1031, Aug 1990.

[5] A. Niknejad and R. Meyer, "Analysis, design, and optimization of spiral inductors and transformers for si rf ics," *Solid-State Circuits, IEEE Journal of*, vol. 33, no. 10, pp. 1470–1481, Oct 1998.

[6] C. Yue and S. Wong, "Physical modeling of spiral inductors on silicon," *Electron Devices, IEEE Transactions on*, vol. 47, no. 3, pp. 560–568, Mar 2000.

[7] A. Scuderi, T. Biondi, E. Ragonese, and G. Palmisano, "A lumped scalable model for silicon integrated spiral inductors," *Circuits and Systems I: Regular Papers, IEEE Transactions on*, vol. 51, no. 6, pp. 1203–1209, June 2004.

[8] K. Tong and C. Tsui, "A physical analytical model of multilayer on-chip inductors," *Microwave Theory and Techniques, IEEE Transactions on*, vol. 53, no. 4, pp. 1143–1149, April 2005.

[9] J. Sieiro, J. LoÌĄpez-Villegas, J. Cabanillas, J. Osorio, and J. Samitier, "A physical frequency-dependent compact model for rf integrated inductors," *Microwave Theory and Techniques, IEEE Transactions on*, vol. 50, no. 1, pp. 384–392, Jan 2002.

[10] J. Gil and H. Shin, "Simple wide-band on-chip inductor model for silicon-based rf ics," in *Simulation of Semiconductor Processes and Devices, 2003. SISPAD 2003. International Conference on*, Sept 2003, pp. 35–38.

[11] Y. Cao, R. Groves, X. Huang, N. Zamdmer, J.-O. Plouchart, R. Wachnik, T.-J. King, and C. Hu, "Frequency-independent equivalent-circuit model for on-chip spiral inductors," *Solid-State Circuits, IEEE Journal of*, vol. 38, no. 3, pp. 419–426, Mar 2003.

[12] X. Huo, P. C. Chan, K. Chen, and H. Luong, "A physical model for on-chip spiral inductors with accurate substrate modeling," *Electron Devices, IEEE Transactions on*, vol. 53, no. 12, pp. 2942–2949, Dec 2006.

[13] A. Watson, D. Melendy, P. Francis, K. Hwang, and A. Weisshaar, "A comprehensive compact-modeling methodology for spiral inductors in silicon-based rfics," *Microwave Theory and Techniques, IEEE Transactions on*, vol. 52, no. 3, pp. 849–857, March 2004.

[14] F. Huang, J. Lu, N. Jiang, X. Zhang, W. Wu, and Y. Wang, "Frequency-independent asymmetric double- π equivalent circuit for on-chip spiral inductors: Physics-based modeling and parameter extraction," *Solid-State Circuits, IEEE Journal of*, vol. 41, no. 10, pp. 2272–2283, Oct 2006.

[15] C. Wang, H. Liao, C. Li, R. Huang, W. Wong, X. Zhang, and Y. Wang, "A wide-band predictive double-π equivalent-circuit model for on-chip spiral inductors," *Electron Devices, IEEE Transactions on*, vol. 56, no. 4, pp. 609–619, April 2009.

[16] M. del Mar Hershenson, S. Mohan, S. Boyd, and T. Lee, "Optimization of inductor circuits via geometric programming," in *Design Automation Conference, 1999. Proceedings. 36th*, 1999, pp. 994–998.

[17] P. Pereira, M. Fino, and F. Coito, "Using discrete-variable optimization for cmos spiral inductor design," in *Microelectronics (ICM), 2009 International Conference on*, Dec 2009, pp. 324–327.

[18] Y. Zhan and S. Sapatnekar, "Optimization of integrated spiral inductors using sequential quadratic programming," in *Design, Automation and Test in Europe Conference and Exhibition, 2004. Proceedings*, vol. 1, Feb 2004, pp. 622–627 Vol.1.

[19] H. B. Dwight, "Geometric mean distances for rectangular conductors," *Electrical Engineering*, vol. 65, no. 8-9, pp. 536–538, Aug 1946.

[20] F. Grover, *Inductance Calculations: Working Formulas and Tables*, ser. Dover phoenix editions. Dover Publications, 1946. [Online]. Available: https://books.google.com/books?id=K3KHi9lIltsC

[21] H. Greenhouse, "Design of planar rectangular microelectronic inductors," *Parts, Hybrids, and Packaging, IEEE Transactions on*, vol. 10, no. 2, pp. 101–109, Jun 1974.

[22] S. Mohan, M. del Mar Hershenson, S. Boyd, and T. Lee, "Simple accurate expressions for planar spiral inductances," *Solid-State Circuits, IEEE Journal of*, vol. 34, no. 10, pp. 1419–1424, Oct 1999.

[23] D. Montgomery and J. Terrell, *Some useful information for the design of air-core solenoids: Part I: Relationships between magnetic field, power, ampere-turns and current density. Part II: Homogenous magnetic fields*, ser. AFOSR-1525. National Magnet Laboratory, Massachusetts Institute of Technology, 1961. [Online]. Available: https://books.google.com/books?id=HDdUAAAAYAAJ

[24] X. Nan and C. Sullivan, "Simplified high-accuracy calculation of eddy-current loss in round-wire windings," in *Power Electronics Specialists Conference, 2004. PESC 04. 2004 IEEE 35th Annual*, vol. 2, June 2004, pp. 873–879 Vol.2.

[25] J. Ferreira, "Aring;nalytical computation of ac resistance of round and rectangular litz wire windings," *Electric Power Applications, IEE Proceedings B*, vol. 139, no. 1, pp. 21–25, Jan 1992.

[26] H. Wheeler, "Formulas for the skin effect," *Proceedings of the IRE*, vol. 30, no. 9, pp. 412–424, Sept 1942.

[27] C. Holloway and E. F. Kuester, "Dc internal inductance for a conductor of rectangular cross section," *Electromagnetic Compatibility, IEEE Transactions on*, vol. 51, no. 2, pp. 338–344, May 2009.

[28] G. Antonini, A. Orlandi, and C. R. Paul, "Internal impedance of conductors of rectangular cross section," *Microwave Theory and Techniques, IEEE Transactions on*, vol. 47, no. 7, pp. 979–985, Jul 1999.

[29] P. Silvester, "Modal network theory of skin effect in flat conductors," *Proceedings of the IEEE*, vol. 54, no. 9, pp. 1147–1151, Sept 1966.

[30] F. Terman, *Radio engineer's handbook*. McGraw-Hill Book Company, inc., 1943.

[31] N. Kovalevski and B. M. Oliver, "An rc oscillator that covers the 20 cps-20 kc range in a single dial sweep," *HEWLETT-PACKARD JOURNAL*, vol. 8, no. 5, jan 1957.

[32] S. Kim and D. Neikirk, "Compact equivalent circuit model for the skin effect," in *Microwave Symposium Digest, 1996., IEEE MTT-S International*, vol. 3, June 1996, pp. 1815–1818 vol.3.

[33] P. Dowell, "Effects of eddy currents in transformer windings," *Electrical Engineers, Proceedings of the Institution of*, vol. 113, no. 8, pp. 1387–1394, August 1966.

[34] H. Abdelbagi, "Skin and proximity effects in two parallel plates." Master's thesis, Wright State University, 2007.

[35] X. Nan and C. Sullivan, "An improved calculation of proximity-effect loss in high-frequency windings of round conductors," in *Power Electronics Specialist Conference, 2003. PESC '03. 2003 IEEE 34th Annual*, vol. 2, June 2003, pp. 853–860 vol.2.

[36] W. Kuhn and N. Ibrahim, "Analysis of current crowding effects in multiturn spiral inductors," *Microwave Theory and Techniques, IEEE Transactions on*, vol. 49, no. 1, pp. 31–38, Jan 2001.

[37] H. Hasegawa, M. Furukawa, and H. Yanai, "Properties of microstrip line on si-sio2 system," *Microwave Theory and Techniques, IEEE Transactions on*, vol. 19, no. 11, pp. 869–881, Nov 1971.

[38] J. Craninckx and M. Steyaert, "A 1.8-ghz low-phase-noise cmos vco using optimized hollow spiral inductors," *Solid-State Circuits, IEEE Journal of*, vol. 32, no. 5, pp. 736–744, May 1997.

[39] J. Shive, *The properties, physics, and design of semiconductor devices*, ser. Bell Telephone Laboratories series. D. Van Nostrand Co., 1959. [Online]. Available: https://books.google.com/books?id=TB9TAAAAMAAJ

[40] S. Kristiansson, F. Ingvarson, and K. Jeppson, "Compact spreading resistance model for rectangular contacts on uniform and epitaxial substrates," *Electron Devices, IEEE Transactions on*, vol. 54, no. 9, pp. 2531–2536, Sept 2007.

[41] E. Garlinger and H. Stover, "Thermal spreading resistance of ring-geometry diodes," *Electron Devices, IEEE Transactions on*, vol. 17, no. 6, pp. 482–484, Jun 1970.

[42] G. Culbertson and H. Stover, "Theoretical solutions for the thermal spreading resistance of ring-geometry diodes," *Electron Devices, IEEE Transactions on*, vol. 19, no. 8, pp. 986–988, Aug 1972.

[43] A. Zolfaghari, A. Chan, and B. Razavi, "Stacked inductors and transformers in cmos technology," *Solid-State Circuits, IEEE Journal of*, vol. 36, no. 4, pp. 620–628, Apr 2001.

[44] C.-H. Wu, C.-C. Tang, and S.-I. Liu, "Analysis of on-chip spiral inductors using the distributed capacitance model," *Solid-State Circuits, IEEE Journal of*, vol. 38, no. 6, pp. 1040–1044, June 2003.

[45] T. Sakurai and K. Tamaru, "Simple formulas for two- and three-dimensional capacitances," *Electron Devices, IEEE Transactions on*, vol. 30, no. 2, pp. 183–185, Feb 1983.

[46] S.-C. Wong, G.-Y. Lee, and D.-J. Ma, "Modeling of interconnect capacitance, delay, and crosstalk in vlsi," *Semiconductor Manufacturing, IEEE Transactions on*, vol. 13, no. 1, pp. 108–111, Feb 2000.

[47] W. Zhao, X. Li, S. Gu, S. Kang, M. Nowak, and Y. Cao, "Field-based capacitance modeling for sub-65-nm on-chip interconnect," *Electron Devices, IEEE Transactions on*, vol. 56, no. 9, pp. 1862–1872, Sept 2009.

[48] B. Razavi, *RF Microelectronics (2Nd Edition) (Prentice Hall Communications Engineering and Emerging Technologies Series)*, 2nd ed. Upper Saddle River, NJ, USA: Prentice Hall Press, 2011.

[49] Y. Koutsoyannopoulos and Y. Papananos, "Systematic analysis and modeling of integrated inductors and transformers in rf ic design," *Circuits and Systems II: Analog and Digital Signal Processing, IEEE Transactions on*, vol. 47, no. 8, pp. 699–713, Aug 2000.

[50] C. Montgomery, R. Dicke, and E. Purcell, *Principles of Microwave Circuits*, ser. IEE electromagnetic waves series. Institution of Engineering & Technology, 1948.

[51] K. O, "Estimation methods for quality factors of inductors fabricated in silicon integrated circuit process technologies," *Solid-State Circuits, IEEE Journal of*, vol. 33, no. 8, pp. 1249–1252, Aug 1998.

[52] H. Packard, *Operating and Service Manual Q Meter 4342A*, Nov 1986.

[53] J. Long and M. Copeland, "The modeling, characterization, and design of monolithic inductors for silicon rf ic's," *Solid-State Circuits, IEEE Journal of*, vol. 32, no. 3, pp. 357–369, Mar 1997.